Investigations of amplitude and phase excitation profiles in femtosecond coherence spectroscopy

Anand T. N. Kumar, Florin Rosca, Allan Widom, and Paul M. Champion
Department of Physics and Center for Interdisciplinary Research on Complex Systems, Northeastern University, Boston, Massachusetts 02115

(Received 23 August 2000; accepted 10 October 2000)

We present an effective linear response approach to pump–probe femtosecond coherence spectroscopy in the well-separated pulse limit. The treatment presented here is based on a displaced and squeezed state representation for the nonstationary states induced by an ultrashort pump laser pulse or a chemical reaction. The subsequent response of the system to a delayed probe pulse is modeled using closed form nonstationary linear response functions, valid for a multimode vibronically coupled system at arbitrary temperature. When pump–probe signals are simulated using the linear response functions, with the mean nuclear positions and momenta obtained from a rigorous moment analysis of the pump induced (doorway) state, the signals are found to be in excellent agreement with the conventional third-order response approach. The key advantages offered by the moment analysis-based linear response approach include a clear physical interpretation of the amplitude and phase of oscillatory pump–probe signals, a dramatic improvement in computation times, a direct connection between pump–probe signals and equilibrium absorption and dispersion lineshapes, and the ability to incorporate coherence associated with rapid nonradiative surface crossing. We demonstrate these aspects using numerical simulations, and also apply the present approach to the interpretation of experimental amplitude and phase measurements on reactive and nonreactive samples of the heme protein myoglobin. The role played by inhomogeneous broadening in the observed amplitude and phase profiles is discussed in detail. We also investigate overtone signals in the context of reaction driven coherent motion. [DOI: 10.1063/1.1329640]

I. INTRODUCTION

Femtosecond coherence spectroscopy (FCS) is an ultrafast pump–probe technique that allows the experimentalist to create and probe coherent vibrational motions and ultrafast chemical reactions in real time.[1–20] In a typical pump–probe experiment, an ultrashort pump laser pulse is used to excite the sample of interest. The subsequent nonstationary response of the medium is monitored by an optically delayed probe pulse. Owing to the large spectral bandwidth available in a short laser pulse, it can generate nonstationary vibrational states in a molecular system as shown in Fig. 1(a). The subsequent nuclear dynamics modulates the optical response as detected by the probe pulse. Coherent vibrational motion in the ground state has been observed in crystalline and liquid phase systems,[2,12] and in biological specimens having short excited state lifetimes such as bacteriorhodopsin,[8,9] and myoglobin.[14] For molecules that have long-lived excited states, however, the excited state coherence is dominant and has been identified in several dye molecules in solution,[1,6,20] in small molecules in the gas phase,[5,7,10] and in photosynthetic reaction centers.[11,17]

Apart from ''field driven'' coherence directly prepared by the laser fields, vibrational coherence can also be driven by rapid nonradiative processes. For example, if we consider a third electronic state $|f\rangle$ that is coupled nonradiatively to the photoexcited state $|e\rangle$ as in Fig. 1(b), the wave packet created in the excited state by the pump can cross over to $|f\rangle$, leaving a vibrationally coherent product.[15] Figure 1(b) suggests the importance of taking a multidimensional view of the problem, whereby the surface crossing between the reactant excited state $|e\rangle$ and the product state, $|f\rangle$ along the reaction coordinate R is accompanied by the creation of a vibrational coherence along the Q coordinate that is coupled to the nonradiative transition. In earlier work, we have presented expressions for the time-dependent population and first moment evolution of vibrational dynamics following a Landau–Zener surface crossing.[21] These expressions are rigorously valid, provided the quantum yield for the reaction is unity (a condition that holds for NO and CO photolysis from heme proteins).[22–24]

A common theoretical formulation for pump–probe spectroscopy is based on the third-order susceptibility $\chi^{(3)}$ formalism, which provides a unified view of four wave mixing spectroscopies[25–28] with different combinations of fields, irrespective of whether they are continuous wave or pulsed. However, the separation of the pump and probe events is not clear in this formalism, since the pump induced density matrix is implicitly contained in the third-order response functions. Thus, it is also attractive to treat the pump and probe processes separately in the well-separated pulse (WSP) limit. For example, the ''doorway/window'' picture has been developed[28] which can be used to represent the pump and probe events as Wigner phase space wave packets. This readily enables a semiclassical interpretation of pump–probe

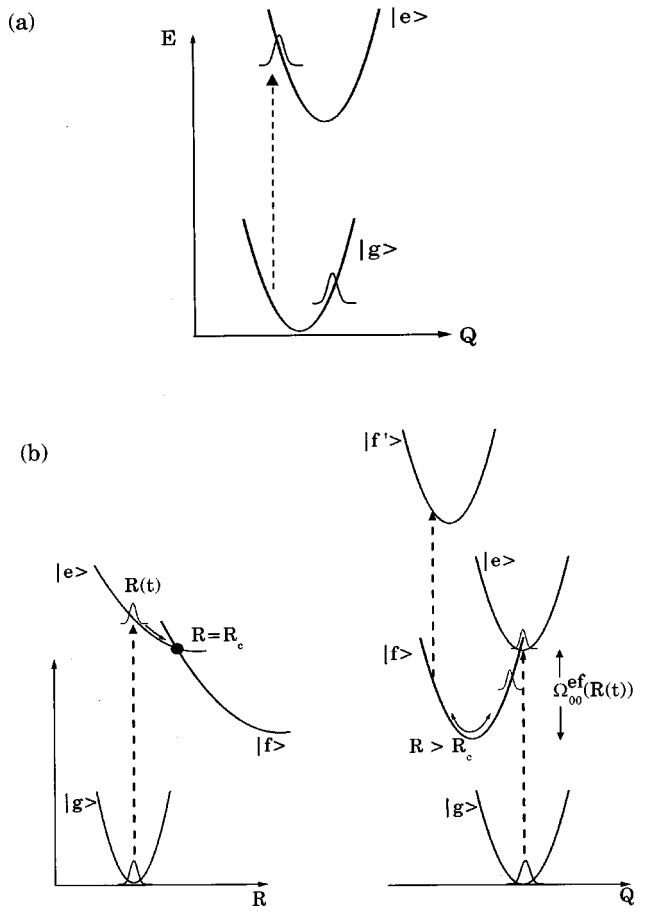

FIG. 1. (a) Schematic of a two-electronic level system, with ground ($|g\rangle$) and excited ($|e\rangle$) electronic states that are coupled radiatively. (b) Multidimensional view of vibrational coherence created by a Landau–Zener surface crossing. Surface crossing along the R-coordinate between the electronic states $|e\rangle$ and $|f\rangle$ leads to vibrational coherence along the Q coordinate in the product electronic state. The states $|g\rangle$ and $|f\rangle$ are assumed not to be radiatively coupled.

experiments.[29–31] Another view of the WSP limit is based on the effective linear response approach. In this approach, the pump induced medium is modeled using a time-dependent linear susceptibility.[32–34,8,27] This has the appealing aspect that a pump–probe experiment is viewed as the nonstationary extension of steady-state absorption spectroscopy.

While the above theoretical treatments are primarily concerned with field driven processes, the need to incorporate additional nonradiative mechanisms into the theory is evident from recent experimental observations.[14,21,35] Recent studies have addressed population transfer during nonadiabatic transitions in electron transfer systems.[36,37] Numerical wave packet propagation techniques have also been presented to model coherent dynamics due to nonadiabatic excited state processes.[38,39]

The present work is motivated by the need to interpret FCS experiments of reactive and nonreactive samples of myoglobin.[35] Here, we make the WSP approximation, and demonstrate the usefulness and accuracy of the effective linear response approach, with the nonstationary states represented using unitary displacement and squeezing operators.[40] This representation readily leads to rigorous analytic expressions for the effective linear response functions. The analytic expressions are physically intuitive and allow for the efficient calculation of oscillatory amplitude and phase profiles over a wide range of carrier frequencies. The resulting information is the FCS analogue of a resonance Raman excitation profile. The computational ease of this approach eliminates the need for impulsive or semiclassical approximations.[39,41–46] Furthermore, when the linear response functions are used in combination with a moment analysis of the pump induced (doorway) state[47] (presented in Appendix A), excellent agreement is found with the full third-order response approach.[27,28] In addition, coherence driven by rapid nonradiative processes as in Fig. 1(b) can be readily incorporated into this formalism. This is illustrated using the first moments (presented in Appendix B) of a Landau–Zener driven coherence.[21]

The general outline of the article is as follows. In Sec. II, we briefly review the third-order response approach and its connection with the effective linear response approach in the well-separated pulse limit. In Sec. III, we obtain analytic expressions for the effective linear response function using a displaced thermal state representation for the doorway state. We further consider undamped vibrational motion and derive arbitrary temperature expressions for the dispersed and open band pump–probe signals. In Sec. IV, we present simulations to demonstrate the accuracy and physically intuitive aspects of the first moment-based effective linear response approach. Next, we include the effects of inhomogeneous broadening of the electronic line shape. Finally, we consider the application of the effective linear response approach to reaction driven coherence, and discuss the magnitude of overtone signals using displaced and squeezed initial states.

II. THIRD-ORDER AND EFFECTIVE LINEAR RESPONSE

Here, we briefly review the connection between the third-order and effective linear response functions in the well-separated pulse limit. In the electric dipole approximation, we ignore the spatial dependence of the electric fields and write the total electric field of the incident pulses as $\mathbf{E}(t)=\mathbf{E}_a(t)+\mathbf{E}_b(t-\tau)$. The subscripts ''$a$'' and ''$b$'' refer to the pump and the probe, and τ is the delay between the two pulses. The detected signal in the open band detection scheme is the differential probe energy transmitted through the medium

$$S(\tau)=-\int_{-\infty}^{+\infty} dt\, \mathbf{E}_b(t-\tau)\cdot(\partial \mathbf{P}(t,\tau)/\partial t), \tag{1}$$

where $\mathbf{P}(t,\tau)$ is the material polarization induced by the pump and probe fields. If we assume that the delay τ is larger than the pulse durations, the lowest order in the polarization that is detected in pump–probe spectroscopy is given by

$$P_i(t,\tau)=\int_{-\infty}^{t} dt_3 \int_{-\infty}^{t_3} dt_2 \int_{-\infty}^{t_2} dt_1\, \chi^{(3)}_{ijkl}(t,t_1,t_2,t_3) \times E_{bj}(t_3-\tau)E_{ak}(t_2)E_{al}(t_1). \tag{2}$$

Here, $\chi^{(3)}_{ijkl}$ is the tensorial third-order susceptibility. We have written the sequential contribution[29] ignoring the coherent

coupling/tunneling terms[18,19] that involve the overlap of the pump and probe fields. The state of the system in between the pump and probe pulses is not exposed in the the above expression for the polarization. If we group the t_1 and t_2 integrations in Eq. (2) that involve only the pump interactions, then we are left with the t_3 integral over the probe field and we may rewrite Eq. (2) as

$$P_i(t,\tau)=\int_{-\infty}^{t} dt_3\, \chi_{ij}^{\mathrm{eff}}(t,t_3)E_{bj}(t_3-\tau), \tag{3}$$

where $\chi_{ij}^{\mathrm{eff}}(t,t_3)$ is the effective linear susceptibility describing the nonstationary medium created by the pump interaction.[27,32] Recall for a stationary medium that $\chi_{ij}^{\mathrm{eff}}(t,t_3)=\chi_{ij}(t-t_3)$, which describes the equilibrium response of the system.

Equations (2) and (3) are formally equivalent expressions for the polarization induced by the well-separated pump and probe pulses. However, Eq. (3) is more important than a mere rephrasing of the third-order polarization expression in the well-separated limit. The nonstationary response function $\chi_{ij}^{\mathrm{eff}}(t,t_3)$ can equally well describe coherence induced by mechanisms other than (and including) the pump field interaction; e.g., a rapid nonradiative surface crossing. To see what is involved, we evaluate the induced polarization quantum mechanically (in the interaction picture[48]) as

$$\mathbf{P}(t)=\mathrm{Tr}(\hat{\rho}(t,\tau)\hat{\mu}(t)), \tag{4}$$

where $\hat{\rho}(t,\tau)$ is density operator describing the quantum-statistical state of the system, and $\hat{\mu}$ is the electric dipole moment operator. We write the total Hamiltonian for the molecule and its interaction with the laser fields as $\hat{H}(t)=\hat{H}_0+\hat{H}_I(t)$, where the free Hamiltonian $\hat{H}_0$ and the interaction Hamiltonian $\hat{H}_I$ have the following form for a molecular system with two electronic levels:

$$\begin{aligned}\hat{H}_0&=\begin{pmatrix}\hat{H}_e+\hbar\Omega_v & 0\\ 0 & \hat{H}_g\end{pmatrix};\\ \hat{H}_I(t)&=-\hat{\mu}\cdot\mathbf{E}(t)=-\begin{pmatrix}0 & \hat{\mu}_{ge}\cdot\mathbf{E}(t)\\ \hat{\mu}_{eg}\cdot\mathbf{E}(t) & 0\end{pmatrix},\end{aligned} \tag{5}$$

where $\hat{H}_g$ and $\hat{H}_e=\hat{H}_g+\hat{V}$, are, respectively, the Born–Oppenheimer Hamiltonians for the ground and excited electronic states. $\hat{V}$ is defined as the difference potential that specifies the electron nuclear coupling and $\hbar\Omega_v$ is the vertical electronic energy gap at the equilibrium position of the ground state. With the above definitions, the third-order susceptibility takes the standard form

$$\begin{aligned}&\chi_{ijkl}^{(3)}(t,t_1,t_2,t_3)\\ &\quad=(i/\hbar)^3\,\mathrm{Tr}(\hat{\mu}_i(t)[\hat{\mu}_j(t_3),[\hat{\mu}_k(t_2),[\hat{\mu}_l(t_1),\hat{\rho}(-\infty)]]]).\end{aligned} \tag{6}$$

Here, $\hat{\rho}(-\infty)$ is the initial density operator of the system before the pump and the probe pulses and Tr denotes the trace operation. Expansion of the above triple commutator leads to four nonlinear response functions and their complex conjugates.[8,28] On the other hand, if we substitute Eq. (6) in Eq. (2), and group the pump field interactions separately, a comparison of the resulting expression with Eq. (3) leads to

$$\begin{aligned}\chi_{ij}^{\mathrm{eff}}(t,t_3)&=(i/\hbar)\mathrm{Tr}(\hat{\mu}_i(t)[\hat{\mu}_j(t_3),\delta\hat{\rho}(t_3)])\\ &=(i/\hbar)\mathrm{Tr}(\delta\hat{\rho}(t_3)[\hat{\mu}_i(t),\hat{\mu}_j(t_3)]).\end{aligned} \tag{7}$$

Here, $\delta\hat{\rho}(t)$ is the perturbation in the density matrix due to the pump interaction (also referred to as the density matrix jump[49] and the doorway function[29,31]) and is given (in the interaction picture) by

$$\begin{aligned}\delta\hat{\rho}(t_3)=\left(\frac{i}{\hbar}\right)^2\int_{-\infty}^{t_3}dt_2\int_{-\infty}^{t_2}dt_1[\hat{\mu}_k(t_2),[\hat{\mu}_l(t_1),\hat{\rho}(-\infty)]]\\ \times E_{ak}(t_2)E_{al}(t_1).\end{aligned} \tag{8}$$

In arriving at the second equality in Eq. (7), we have used the invariance of the trace under permutation. In the WSP limit, where the overlap between the pump and probe pulse is negligible, we can extend the upper limit t_3 in Eq. (8) to infinity. The interaction picture density matrix is then time independent, so that we may drop the time arguments from the density matrix.

Equation (7) expresses the effective linear response as the average value of the standard linear response Green's function[50] with respect to the pump induced (nonstationary) density matrix $\delta\hat{\rho}$. Note that $\delta\hat{\rho}$ does not necessarily have to be induced by the pump fields as in Eq. (8). It could, for example, describe the perturbation in the state of the system due to a nonradiative interaction that follows the pump excitation to a dissociative state. It might even be a pump induced state with higher-order pump interactions included as would be required for very strong pump fields.[51] The only assumptions are that the probe field interrogates the nonstationary medium after the coherence has been created, and that the probe interaction with the medium is linear.

We express the full perturbed density matrix $\delta\hat{\rho}$ in terms of the ground and excited electronic state nuclear submatrices. The point is that the second-order density matrix in Eq. (8) has no electronic coherence due to the even number of dipole interactions. Hence

$$\delta\hat{\rho}=\delta\hat{\rho}_e|e\rangle\langle e|+\delta\hat{\rho}_g|g\rangle\langle g|=\begin{pmatrix}\delta\hat{\rho}_e & 0\\ 0 & \delta\hat{\rho}_g\end{pmatrix}. \tag{9}$$

Correspondingly, the effective linear susceptibility Eq. (7) can be decomposed into a ground and excited state linear response function

$$\chi_{ij}^{\mathrm{eff}}(t,t_3)=\chi_{ij}^{(g)}(t,t_3)+\chi_{ij}^{(e)}(t,t_3), \tag{10}$$

where

$$\chi_{ij}^{(s)}(t,t_3)=(i/\hbar)\mathrm{Tr}[\delta\hat{\rho}_s\langle s|[\hat{\mu}_i(t),\hat{\mu}_j(t_3)]|s\rangle], \tag{11}$$

where $s=g$ or e.

In general, the pulse induced nuclear density matrices $\delta\hat{\rho}_g$ and $\delta\hat{\rho}_e$ contain vibrational coherence, i.e., off-diagonal elements in the phonon number state representation. This coherence translates into time-dependent wave packets in a semiclassical phase space (Q,P) Wigner representation of the density matrix.[31,52,53,28] On the other hand, the highly localized (in Q and P) nature of the impulsively excited nonstationary states suggests that we calculate their moments using

$$\overline{X}_s(t)=\mathrm{Tr}[\langle s|\hat{X}(t)|s\rangle\,\delta\hat{\rho}_s]/\mathrm{Tr}[\hat{\rho}_s]. \tag{12}$$

With $\hat{a}^\dagger(\hat{a})$ as the creation (destruction) operator for the phonon mode, $\hat{X}$ represents the dimensionless quadrature operators $\hat{Q}=(\hat{a}^\dagger+\hat{a})/\sqrt{2}$, $\hat{P}=i(\hat{a}^\dagger-\hat{a})/\sqrt{2}$ or their higher powers. The time t is larger than the pulse duration. Let the initial $(t=0)$ values of the first moments of the position $\overline{Q}_s(0)$ and momentum $\overline{P}_s(0)$, for (say) $s=e$ or $s=g$ be denoted by (Q_{s0},P_{s0}). These uniquely determine the subsequent first moment dynamics $\overline{Q}_s(t)$. Since Q_{s0} and P_{s0} denote shifts from thermal equilibrium, we may represent the pump induced nuclear density matrix for the electronic state s as

$$\delta\hat{\rho}_s=\hat{D}(\lambda_s)\hat{\rho}_T^{(s)}\hat{D}^\dagger(\lambda_s), \tag{13}$$

where $\hat{\rho}_T^{(s)}$ is the equilibrium thermal density matrix corresponding to the electronic level s,

$$\hat{\rho}_T^{(s)}=Z_s^{-1}\exp(-\hat{H}_s/k_BT). \tag{14}$$

$\hat{D}(\lambda_s)$ is the quantum mechanical displacement operator[54] defined as

$$\hat{D}(\lambda_s)=\exp(\lambda_s\hat{a}^\dagger-\lambda_s^*\hat{a}). \tag{15}$$

Here $\lambda_s=(Q_{s0}+iP_{s0})/\sqrt{2}$ is the initial displacement (in phase space) of the coherent state induced on the potential surface s. When Eq. (13) is substituted into Eq. (11), the response functions $\chi^{(e,g)}$ are readily calculated as we show below. Furthermore, Eq. (13) offers a general scheme to represent the nonstationary density matrix on any given electronic level with only a knowledge of the first moment λ_s. The effective linear response function is thus not restricted to coherences driven by a second-order pump interaction. This is the point of departure of the present work from earlier treatments[32,33,8,27] which generally utilize the second-order pump induced density matrix Eq. (8), and are thus formally identical to the $\chi^{(3)}$ approach. This development can be extended to include the higher moments of $\hat{Q}$ and $\hat{P}$, but for harmonic potentials we expect the higher moments to play a less significant role in the overall dynamics. Second moment changes are incorporated in a manner analogous to Eq. (13) in Appendix D.

A. Detection schemes

The two common experimental detection schemes are the open band and the dispersed probe configurations. For simplicity, we assume that the medium is isotropic and take the pulse fields to be scalar quantities. We then write the susceptibilities without tensor subscripts. The measured open band signal is given by Eq. (1). For an almost monochromatic laser pulse, we can write the electric field and the induced polarization as

$$\begin{aligned} &E_b(t-\tau)=\Re e\{\mathcal{E}(t-\tau)e^{-i\omega_c(t-\tau)}\} \quad \text{and}\\ &P(t,\tau)=\Re e\{\mathcal{P}(t,\tau)e^{-i\omega_c(t-\tau)}\}, \end{aligned} \tag{16}$$

where ω_c is the carrier frequency, and $\mathcal{E}(t-\tau)$ and $\mathcal{P}(t,\tau)$ are slowly varying envelope functions. Typically, the envelope function for the probe field is a real Gaussian centered at time τ; $\mathcal{E}(t-\tau)=E_0G(t-\tau)$, where E_0 is the field strength of the probe pulse. The envelope function for the polarization can be obtained by using the definitions in Eq. (16) and Eq. (3). After making a change of variables $s=t-t_3$, we find

$$\mathcal{P}(t,\tau)=\int_0^\infty ds\, e^{i\omega_c s}\chi^{\mathrm{eff}}(t,t-s)\mathcal{E}(t-s-\tau). \tag{17}$$

Employing Eqs. (16)–(17) in Eq. (1), and making the rotating wave approximation (RWA) in which highly oscillating nonresonant terms are ignored, we get

$$S(\tau)=-(\omega_c/2)\Im m\int_{-\infty}^\infty dt\,\mathcal{E}^*(t-\tau)\mathcal{P}(t,\tau). \tag{18}$$

Since for the present case $\mathcal{E}(t)$ is real, the measured (dichroic) signal is directly related to $\Im m\{\mathcal{P}(t,\tau)\}$. If $\mathcal{E}(t)$ were made imaginary as in heterodyne techniques,[55,41] then the resulting (birefringent) signal is related $\Re e\{\mathcal{P}(t,\tau)\}$.

In the dispersed probe detection scheme, the measured quantity is the spectral density $\tilde{S}(\omega,\tau)$ of the transmitted energy through the sample defined by

$$S(\tau)=\int_0^\infty \tilde{S}(\omega,\tau)d\omega. \tag{19}$$

In the RWA,

$$\begin{aligned} \tilde{S}(\omega,\tau)=&-(\omega/4\pi)\Im m\{e^{-i(\omega-\omega_c)\tau}\tilde{\mathcal{E}}^*(\omega-\omega_c)\\ &\times\tilde{\mathcal{P}}(\omega-\omega_c,\tau)\}, \end{aligned} \tag{20}$$

where $\tilde{\mathcal{E}}(\omega)$ and $\tilde{\mathcal{P}}(\omega)$ denote the Fourier transforms of the envelope functions, $\mathcal{E}(t)$ and $\mathcal{P}(t,\tau)$.

III. EVALUATION OF THE RESPONSE FUNCTIONS

In this section, we evaluate both the third-order and the effective linear response functions. Consider the ground state response function $\chi_g(t,t_3)$ given by Eq. (11) without the tensor subscripts. We make the Condon approximation and ignore the coordinate dependence of the dipole moment operator. If we then let $\hat{\mu}=\mu_{ge}|g\rangle\langle e|+\mu_{eg}|e\rangle\langle g|$, and use the interaction picture time evolution $\hat{\mu}(t)=e^{i\hat{H}_0t/\hbar}\hat{\mu}e^{-i\hat{H}_0t/\hbar}$, we can write

$$\chi_g(t,t_3)=(i|\mu_{ge}|^2/\hbar)[C_g(t,t_3)-C_g^*(t,t_3)], \tag{21}$$

where we have defined the two-time correlation function for the ground state response,

$$C_g(t,t_3)=e^{-i\Omega_v(t-t_3)}\mathrm{Tr}\left[\delta\hat{\rho}_g\exp\left(-\frac{i}{\hbar}\int_{t_3}^t ds\,\hat{V}(s)\right)_+\right]. \tag{22}$$

Here, the subscript + denotes time ordering and $\hat{V}(s)$ evolves in time s via $\hat{H}_g$. The density matrix $\delta\hat{\rho}_g$ is obtained from Eq. (8) as $\langle g|\delta\hat{\rho}|g\rangle$, assuming $\hat{\rho}(-\infty)=\hat{\rho}_T^{(g)}|g\rangle\langle g|$:

$$\delta\hat{\rho}_g = -\frac{|\mu_{ge}|^2}{\hbar^2}\int_{-\infty}^{\infty} dt_2 \int_{-\infty}^{t_2} dt_1\, E_a(t_2)E_a(t_1) \times\left\{ e^{-i\Omega_v(t_2-t_1)} \exp\left(-\frac{i}{\hbar}\int_{t_1}^{t_2} ds\, \hat{V}(s)\right)_+ \hat{\rho}_T^{(g)} + \text{h.c.}\right\}, \tag{23}$$

where h.c. denotes Hermitian conjugate.

For the excited state response function, we similarly write

$$\chi_e(t,t_3) = (i|\mu_{ge}|^2/\hbar)[C_e(t,t_3) - C_e^*(t,t_3)], \tag{24}$$

where C_e is the two-time correlation function for the excited state response:

$$C_e(t,t_3) = e^{i\Omega_v(t-t_3)}\text{Tr}\left[\delta\hat{\rho}_e \exp\left(\frac{i}{\hbar}\int_0^t ds\, \hat{V}(s)\right)_- \times\exp\left(-\frac{i}{\hbar}\int_0^{t_3} ds\, \hat{V}(s)\right)_+\right], \tag{25}$$

with the subscript $-$ denoting antitime ordering. The excited state density matrix $\delta\hat{\rho}_e$ is obtained as $\langle e|\delta\hat{\rho}|e\rangle$:

$$\delta\hat{\rho}_e = \frac{|\mu_{ge}|^2}{\hbar^2}\int_{-\infty}^{\infty} dt_2 \int_{-\infty}^{t_2} dt_1\, E_a(t_1)E_a(t_2) \times\left\{ e^{i\Omega_v s} \exp\left(\frac{i}{\hbar}\int_0^{t_2} ds'\, \hat{V}(s')\right)_- \hat{\rho}_T^{(g)} \times\exp\left(-\frac{i}{\hbar}\int_0^{t_1} ds'\, \hat{V}(s')\right)_+ + \text{h.c.}\right\}. \tag{26}$$

The above expressions are valid for a two-level system with arbitrary difference potentials. In what follows, we take $\hat{V} = -(\hbar/m\omega_0)^{1/2} f\hat{Q} = -(\hbar\omega_0\Delta)\hat{Q}$, with dimensionless $\hat{Q}$ and relative displacement Δ. The electron–nuclear coupling force is expressed as $f = \Delta(m\omega_0^3\hbar)^{1/2}$, where m and ω_0 are, respectively, the reduced mass and frequency of the mode.

If the trace in Eqs. (22) and (25) were evaluated with respect to the equilibrium thermal density matrices $\hat{\rho}_T^{(e,g)}$ rather than $\delta\hat{\rho}_{e,g}$, then the correlation functions, $C_{e,g}(t,t_3) = K_{e,g}(t-t_3)$ would be the equilibrium absorption and emission correlators,[56] i.e.,

$$K_g(s) = e^{-i\Omega_{00}s - \Gamma_e|s|}e^{-g(s)}; \quad K_e(s) = e^{i\Omega_{00}s - \Gamma_e|s|}e^{-g(s)}, \tag{27}$$

where we have introduced homogeneous dephasing through the electronic damping constant Γ_e. For linearly displaced and undamped oscillators, $g(s)$ is given by

$$g(s) = (\Delta^2/2)[(2\bar{n}_T + 1)(1 - \cos(\omega_0 s)) + i\sin(\omega_0 s)], \tag{28}$$

where $2\bar{n}_T + 1 = \coth(\hbar\omega_0/2k_BT)$. Exact expressions for the damped harmonic oscillator[57] can be easily incorporated into the present development. The half-Fourier transforms of $K_{e,g}(t)$ determine complex line shape functions,

$$\Phi(\omega) = i\int_0^{\infty} ds\, e^{i\omega s}K_g(s), \quad \text{and}$$
$$\Theta(\omega) = i\int_0^{\infty} ds\, e^{i\omega s}K_e^*(s), \tag{29}$$

whose imaginary parts are directly related to the absorption and emission cross section, $\sigma_A(\omega) \propto \omega\Phi_I(\omega)$ and $\sigma_F(\omega) \propto \omega^3\Theta_I(\omega)$.

A. Full third-order response

Analytic expressions have been derived for the third-order susceptibility $\chi^{(3)}$ for a two-level system coupled to a multimode set of linearly displaced harmonic oscillators, and expressed in terms of nonlinear response functions R_j $(j = 1..4)$.[26,28] For completeness, these are listed in Appendix C. When the second-order pump induced density matrices in Eqs. (23) and (26) are substituted in Eqs. (22) and (25), the ground and excited state correlation functions $C_{g,e}$ are related to the nonlinear response functions as expressed in Eqs. (C1) and (C4).

The expressions of Appendix C cast the effective linear response functions in terms of the conventional nonlinear response functions. The two approaches are entirely equivalent at this stage. The key point from Eqs. (C1) and (C4) is that the ground and excited state correlation functions $C_{g,e}(t,t_3)$ involve a double integration over the pump electric fields. In the next section, we will show that the displaced state representation for the nonstationary density matrix Eq. (13) directly leads to analytic expressions for $C_{g,e}(t,t_3)$.

B. Effective linear response

1. Displaced thermal state

Following Eq. (13), we represent the pump induced nonstationary state as

$$\delta\hat{\rho} = \hat{D}(\lambda_g)\hat{\rho}_T^{(g)}\hat{D}^\dagger(\lambda_g)|g\rangle\langle g| + \hat{D}(\lambda_e)\hat{\rho}_T^{(e)}\hat{D}^\dagger(\lambda_e)|e\rangle\langle e|. \tag{30}$$

This representation can be used to calculate the effective linear response in a straightforward manner.[58] Substituting the ground state part of Eq. (30) into the correlation function in Eq. (22) and using the permutation invariance of the trace and the unitarity of the displacement operator, we obtain

$$C_g(t,t_3) = e^{-i\Omega_v(t-t_3)}Tr\left[\hat{\rho}_T^{(g)} \exp\left(i\omega_0\Delta\int_{t_3}^{t} ds\, \hat{D}^\dagger(\lambda_g) \times\hat{Q}(s)\hat{D}(\lambda_g)\right)_+\right]. \tag{31}$$

The effect of the displacement operator is to shift the position operator by a time-dependent classical function (c-number), namely the mean pump induced displacement:[40]

$$\hat{D}^\dagger(\lambda_g)\hat{Q}(s)\hat{D}(\lambda_g) = \hat{Q}(s) + \overline{Q}_g(s), \tag{32}$$

where $\overline{Q}_g(s) = \sqrt{2}\Re e\{\lambda_g e^{-i\omega_0 s}\}$ is the time-dependent mean position of the oscillator in the ground state. If we substitute the above expression into Eq. (31), then the c-number $\overline{Q}_g(s)$

can be removed outside the time ordering and the thermal average simply reduces to the equilibrium absorption correlator $K_g(t-t_3)$ in Eq. (27). Using Eq. (A3) of Appendix A for the first moment dynamics, we find

$$C_g(t,t_3)=K_g(t-t_3)\exp\Bigg(i\omega_0 A_g\Delta\int_{t_3}^{t} ds\, e^{-\gamma|s|} \times\cos(\omega_v s+\varphi_g)\Bigg), \tag{33}$$

where $A_g=\sqrt{2}|\lambda_g|$ and $\varphi_g=\arg(\lambda_g^*)=-\tan^{-1}(P_{g0}/Q_{g0})$ are the amplitude and phase for the coherent wave packet motion in the ground electronic state. The above expression has an intuitively appealing form: the ground state correlation function for the pump induced nonstationary medium is expressed as a modulation of the standard equilibrium (linear) absorption correlator[56] $K_g(t-t_3)$ by the first moment dynamics of the ground state wave packet motion. It is clear that the corresponding nonstationary ground state response function $\chi_g(t,t_3)$, Eq. (21), would translate in the frequency domain into dynamic absorption and dispersion lineshapes,[32,8,27] which determine the final probe response to the nonstationary medium. After performing the integral, Eq. (33) reads

$$C_g(t,t_3)=K_g(t-t_3)\exp[\,i(A_g\Delta/\omega_0)\{e^{-\gamma t}(\omega_v\sin(\omega_v t+\varphi_g) -\gamma\cos(\omega_v t+\varphi_g))-e^{-\gamma t_3}(\omega_v\sin(\omega_v t_3+\varphi_g) -\gamma\cos(\omega_v t_3+\varphi_g))\}]. \tag{34}$$

It is interesting to note that the strength of the first moment modulation appears through the product of the initial displacement and the optical coupling, $A_g\Delta$.

For the excited state correlation function, we similarly find

$$C_e(t,t_3)=K_e(t-t_3)\exp[\,-i(A_e\Delta/\omega_0) \times\{e^{-\gamma t}(\omega_v\sin(\omega_v t)-\gamma\cos(\omega_v t)) -e^{-\gamma t_3}(\omega_v\sin(\omega_v t_3)-\gamma\cos(\omega_v t_3))\}]. \tag{35}$$

Thus, the excited state nonequilibrium correlation function is expressed as a modulation of the equilibrium fluorescence correlation function by the excited state wave packet.

The analytic expressions in Eqs. (34) and (35) together with the first moments presented in Eqs. (A1), (A2), and (A4), effectively replace the nonlinear response expressions derived in Eqs. (C1) and (C4). The generalization of the above single mode results to the multimode case is straightforward. It easy to show that the multimode expressions for C_g and C_e factor into a product of single mode correlation functions. The results derived using the first moments are approximate, since the higher moments of the wave packet motion (which are induced by the pump pulse[47]) are neglected. Nevertheless, they provide a fully quantum mechanical description of the probe response due to modulation by coherent nuclear dynamics. Moreover, we expect that for a harmonic system, the first moment dynamics will constitute a major part of the wave packet motion detected by the probe. This expectation is verified when we present simulations comparing the first moment based linear response approach with the full third-order approach.

2. Analytic expressions for pump–probe signal: CARS and CSRS responses

An advantage of the analytic expressions in Eqs. (34) and (35) is that for the special case of undamped nuclear motion, they can be expanded in a Fourier–Bessel series, from which the polarization Eq. (17) can be evaluated in closed form. This yields an analytic expression for the dispersed probe signal Eq. (20) that provides insight into the origin of both resonant and nonresonant pump–probe signals. If the series expansion

$$e^{i\varrho\,\sin(\theta)}=\sum_{m=-\infty}^{\infty}\exp(im\theta)J_m(\varrho), \tag{36}$$

is placed into Eq. (34), we find for $\gamma=0$ that

$$C_g(t,t_3)=K_g(t-t_3)\sum_{k=-\infty}^{\infty}e^{ik(\omega_0 t_3+\varphi_g)}\sum_{n=-\infty}^{\infty}J_n(A_g\Delta) \times J_{n-k}(A_g\Delta)e^{in\omega_0(t-t_3)}. \tag{37}$$

We put this expression into Eqs. (21) and (17) to find the polarization within the RWA (which neglects the contribution of C_g^*). With Gaussian pulses, $\tilde{\mathcal{E}}(\omega)=E_0\tilde{G}(\omega)$, where $\tilde{G}(\omega)$ is a Gaussian spectral function. The ground state contribution to the frequency dispersed pump–probe signal is finally obtained:

$$\tilde{S}_g(\omega,\tau)=\sum_{k=0}^{\infty}[\mathcal{C}_k(\omega)\cos(k(\omega_0\tau+\varphi_g)) +\mathcal{S}_k(\omega)\sin(k(\omega_0\tau+\varphi_g))] \tag{38a}$$

$$=\sum_{k=0}^{\infty}\tilde{A}_k(\omega)\cos(k\omega_0\tau+\tilde{\phi}_k(\omega)), \tag{38b}$$

where the amplitude and phase of the kth overtone are

$$\tilde{A}_k(\omega)=[\mathcal{C}_k^2(\omega)+\mathcal{S}_k^2(\omega)]^{1/2}, \tag{39a}$$

$$\tilde{\phi}_k(\omega)=k\varphi_g-\tan^{-1}[\mathcal{S}_k(\omega)/\mathcal{C}_k(\omega)], \tag{39b}$$

and where $\mathcal{C}_k(\omega)$ and $\mathcal{S}_k(\omega)$ are the quadrature amplitudes given by

$$\mathcal{C}_k(\omega)=\omega M[\tilde{G}_p(\omega_d,k\omega_0)\Phi_I^{(k)}(\omega) +\tilde{G}_p(\omega_d,-k\omega_0)\Phi_I^{(-k)}(\omega)], \tag{40a}$$

$$\mathcal{S}_k(\omega)=\omega M[\tilde{G}_p(\omega_d,k\omega_0)\Phi_R^{(k)}(\omega) -\tilde{G}_p(\omega_d,-k\omega_0)\Phi_R^{(-k)}(\omega)]. \tag{40b}$$

In the above expressions, we have defined the constant $M=-(|\mu_{ge}|^2E_0^2/4\pi\hbar)$ for convenience, and introduced the product spectral function of the probe pulse,

$$\tilde{G}_p(\omega_d,k\omega_0)=\tilde{G}(\omega_d)\tilde{G}(\omega_d+k\omega_0), \tag{41}$$

where $\omega_d=\omega-\omega_c$ is the detuning frequency, and the absorptive and dispersive basis functions are defined as

$$\Phi_I^{(k)}(\omega)=\sum_{n=-\infty}^{\infty} J_n(A_g\Delta)J_{n-k}(A_g\Delta)\Phi_I(\omega+n\omega_0), \quad (42a)$$

$$\Phi_R^{(k)}(\omega)=\sum_{n=-\infty}^{\infty} J_n(A_g\Delta)J_{n-k}(A_g\Delta)\Phi_R(\omega+n\omega_0). \quad (42b)$$

The basis functions depend only on A_g, Δ, and the equilibrium line shape functions and do not depend on the properties of the probe pulse. Note the symmetry conditions $\Phi_I^{(-k)}(\omega)=\Phi_I^{(k)}(\omega-k\omega_0)$ and $\Phi_R^{(-k)}(\omega)=\Phi_R^{(k)}(\omega-k\omega_0)$. Equations (38)–(42) are rigorous expressions for the dispersed probe signal for a single undamped mode coupled to a two-electronic level system. They are valid for arbitrary temperature, detection frequency, and pulse width. The simple and direct connection between pump–probe signals and the equilibrium line shape functions is exposed by these results. Equilibrium line shapes thus enter the calculation at two separate stages: firstly in the expressions for the pump induced first moment amplitude and phase in Eqs. (A1) and (A2), and secondly in the final probe detected signal in Eqs. (42a)–(42b).

It is clear from Eqs. (38) that the detuning dependence of the dispersed probe signal is determined by the amplitudes $\mathcal{C}_k(\omega)$ and $\mathcal{S}_k(\omega)$, which are in turn related to the product of the spectral function $\tilde{G}_p$ and the displaced line shape functions $\Phi_{I,R}^{(k)}$. In studying the detuning dependence of $\tilde{S}_g(\omega,\tau)$, it is interesting to look at two opposite limits. When the electronic dephasing time is much longer than the pulse durations and the vibrational periods, the basis functions $\Phi_I^{(k)}(\omega)$ and $\Phi_R^{(k)}(\omega)$ consist of a well-resolved Franck–Condon progression that acts like a filter in Eqs. (40a) and (40b) and determines the detuning dependence. In the opposite limit, the electronic dephasing time is much shorter than the pulse durations and vibrational periods. In this case, the line shape functions are broad, exhibiting a much slower variation with respect to ω than the pulse envelope spectral function which then acts like a filter in Eqs. (40a) and (40b). The dispersed signal then consists of a superposition of red and blue shifted field envelope functions $\tilde{G}_p(\omega_d,\pm k\omega_0)$. The superposition weighting depends on the amplitude of the initial pump induced displacement and the displaced equilibrium line shape functions. Thus, resonances occur at frequencies $\omega\approx\omega_c\mp k\omega_0/2$, which correspond to the peaks of $\tilde{G}_p(\omega_d,\pm k\omega_0)$. These resonances can be identified with the well-known coherent Stokes Raman scattering (CSRS) and coherent antiStokes Raman scattering (CARS) signals.[59,60]

The delay dependence of the dispersed signal is composed of oscillations at all harmonics of the fundamental frequency ω_0. The amplitude and the phase of the kth harmonic is given by $\tilde{A}_k(\omega)$ and $\tilde{\phi}_k(\omega)$. It is clear from Eq. (39b) that the dispersed probe signal phase $\tilde{\phi}_k(\omega)$ is not simply related to the initial phase φ_g of the coherent motion because of the additional frequency dependent functions $\mathcal{C}_k(\omega)$ and $\mathcal{S}_k(\omega)$. However, it can be easily shown that when we integrate $\tilde{S}_g(\omega,\tau)$ as specified in Eq. (19), the integral over $\mathcal{S}_k(\omega)$ is small due to approximately canceling contributions from the Stokes and antiStokes shifted components in Eq. (40b). We then get for the ground state contribution to the open band signal

$$S_g(\tau)=\sum_{k=0}^{\infty} A_{sk}\cos(k\omega_0\tau+\phi_{sk}), \quad (43)$$

where the amplitude and phase of the kth overtone are given by

$$A_{sk}=\int_0^{\infty} d\omega|\mathcal{C}_k(\omega)|, \quad (44a)$$

$$\phi_{sk}=k\varphi_g-[0 \text{ or } \pi]. \quad (44b)$$

Thus, the phase of the fundamental open band signal ϕ_{s1} determines the initial phase φ_g of the nuclear motion to within an additive constant of π. The additive constant phase arises from the fact that $\mathcal{C}_k(\omega)$ can have positive or negative values. This in turn reflects the fact that the measured oscillatory signal is the transmission of the probe pulse rather than the mean wavepacket position itself. [See Fig. 3 and the related discussion.] It is easily shown that the open band signal will be of the form in Eq. (43) even when several vibrational modes are active. These results demonstrate that the phases of the open band signals are a direct reflection of the initial conditions of the nonstationary states.

It is also notable from Eqs. (43)–(44) that the open band (dichroic) signal vanishes as we tune off-resonance,[61] where the imaginary line shape function is negligible and $\mathcal{C}_k(\omega)$ is vanishingly small. In contrast, the off-resonant frequency dispersed signal is nonvanishing and depends on the real part of the line shape through $\mathcal{S}_k(\omega)$. We also have $\varphi_g=\pi/2$ off-resonance using the results of Appendix A. We then get

$$\tilde{S}_g(\omega,\tau)=\sum_{k=0}^{\infty} \mathcal{S}_k(\omega)\sin(k(\omega_0\tau+\pi/2)). \quad (45)$$

The dispersive functions $\Phi_R^{(k)}(\omega)$ are approximately constant in the off-resonant limit. It then follows from Eq. (40b) that the detuning dependence is mainly determined by the pulse spectral function $\tilde{G}_p$. The dispersed probe signal consists of CARS and CSRS resonances that are centered near $\omega\approx\omega_c\mp k\omega_0/2$ and oppositely phased.[60,62]

The expressions derived here make minimal assumptions and can be readily extended to incorporate optical heterodyne detection schemes.[42,43,55,62] We have derived explicit expressions for the dichroic response $\Im m\{\mathcal{P}(t,\tau)\}$. It can be shown for the birefringent response $\Re e\{\mathcal{P}(t,\tau)\}$, that the roles of the quadrature amplitudes in Eq. (38a) will be reversed; i.e., that $\mathcal{C}_k(\omega)$ is the coefficient of the sine term and $\mathcal{S}_k(\omega)$ is the coefficient of the cosine term. Also, the CARS and CSRS contributions of $\mathcal{S}_k(\omega)$ will add constructively to give a nonvanishing birefringent open band signal off-resonance. This has been observed in transparent liquids.[62] For the resonant case, the results derived here are a multilevel, high temperature generalization of earlier treatments based on density matrix pathways[55] which considered a pair of vibrational levels in the ground and excited states. In contrast to prior treatments,[42,43] no assumption has been made

with regard to the pulse durations in deriving Eqs. (38)–(42). Finally, we note that although we have given expressions for only the ground state response, analogous results are easily obtained for the excited state response. Here, the emission line shape function $\Theta(\omega)$ in Eq. (29) plays a role similar to $\Phi(\omega)$ in the ground state expressions.

3. Reaction driven coherence

As previously discussed, an advantage of the effective linear response approach is that it allows for a rigorous calculation of the probe response to nonradiatively driven coherence. As an example, we consider the multilevel system depicted in Fig. 1(b), and apply the effective linear response approach to the detection of reaction induced coherent nuclear motion along the Q degree of freedom in the product state $|f\rangle$.

The chemical reaction step and subsequent probe interaction minimally constitute a three-electronic level problem comprising the electronic states $|e\rangle$, $|f\rangle$, and $|f'\rangle$. The states $|e\rangle$ and $|f\rangle$ are nonradiatively coupled. The probe interaction couples the ground state $|f\rangle$ and excited state $|f'\rangle$ of the product, and is assumed to be well-separated from the reaction step. The Hamiltonian for the reaction-probe stage of the problem may be written as

$$\hat{H}_{\mathrm{NR}}(t)=\begin{pmatrix} \Omega_v^f+\hat{H}_{f'} & -\mu_{ff'}E_b(t) & 0 \\ -\mu_{f'f}E_b(t) & \hat{H}_f+U_f(R) & J \\ 0 & J & \hat{H}_e+U_e(R) \end{pmatrix}. \tag{46}$$

Here, $U_{e,f}$ are the dissociative potentials along the classical reaction coordinate R, for the states $|e\rangle$ and $|f\rangle$. $\hat{H}_{e,f}$ represent the quantum degree of freedom (Q) coupled to the nonradiative transition. J is the nonradiative coupling parameter which, for the case of MbNO photolysis discussed below, corresponds to the spin–orbit coupling operator needed to account for the spin change of the heme iron atom upon ligand photolysis. For simplicity, we also assume that the pump interaction that couples the states $|g\rangle$ and $|e\rangle$ is well separated from the chemical reaction. The sequence of interactions and the relevant coupling constants is then pump, $\mu E_a \rightarrow$ chemical reaction, $J\rightarrow$ and probe, μE_b. Each individual interaction is assumed to occur independently. The separation of these events allows us to consider the four-electronic level problem in Fig. 1(b) as three sequential two-electronic level problems.

We make the following two assumptions which are satisfied in the case of MbNO photolysis: (i) before the curve crossing takes place, the system (in reactant state $|e\rangle$) is assumed be in thermal equilibrium along the Q coordinate, (ii) the quantum yield for the dissociative reaction along R is assumed to be unity, i.e., all the reactant molecules are transferred to the product state during the surface crossing. Assumption (i) holds if the Q coordinate is not optically coupled to the $|g\rangle$ and $|e\rangle$ electronic states. The pump pulse merely transports a fraction of the ground state electronic population to the excited state, leaving the vibrational state along Q unchanged. However, the R degree of freedom is dissociative on the excited state potential surface and is left far from equilibrium after the pump excitation. For example, the $220\,\mathrm{cm}^{-1}$ Fe–His mode in MbNO is not optically coupled as revealed by its absence in the resonance Raman spectrum of MbNO. Its strong presence in the pump–probe signals demonstrates that this mode is triggered into oscillation following the highly efficient process[22–24] of ligand photodissociation in MbNO.[14]

A multidimensional Landau–Zener theory was previously developed to describe vibrational coherence induced by nonradiative electronic surface crossing[21] based on assumptions (i) and (ii) above. For completeness of presentation, we have reproduced the key results of that work in Appendix B. We also present expressions for the amplitude A_f and phase φ_f of the first moment of the nuclear motion induced on the product surface $|f\rangle$. Using these reaction driven initial conditions, we make the following representation for the nonstationary nuclear density matrix in the product state $\hat{\rho}_f'$:

$$\hat{\rho}_f'=\hat{D}(\lambda_f)\hat{\rho}_T^{(f)}\hat{D}^{\dagger}(\lambda_f), \tag{47}$$

where $\lambda_f=A_f e^{i\varphi_f}/\sqrt{2}$ is the complex displacement of the reaction induced coherence and $\hat{\rho}_T^{(f)}$ is the equilibrium thermal density matrix for the nuclear Hamiltonian $\hat{H}_f$. Since only the ground state of the product $|f\rangle$ is initially populated, the probe response due to the nuclear dynamics in the product state potential well can now be obtained along the same lines that led to Eq. (34). The correlation function C_f for the nonstationary response is obtained by replacing A_g, φ_g, and Δ by A_f, φ_f, and Δ_f in Eq. (34). Here Δ_f is the dimensionless displacement associated with the coupling of Q to the $f\rightarrow f'$ transition. The equilibrium optical absorption correlator is replaced by $K_f(t-t_3)$, which refers to the pair of electronic states $|f\rangle$ and $|f'\rangle$.

IV. SIMULATIONS AND DISCUSSION

The numerical simulation of the open band signals involves multiple integrals of the time correlation functions which can be evaluated using standard algorithms. The full third-order response approach involves quadruple integrations over time. The effective linear response approach replaces the correlation functions in Eq. (C1) and (C4) by the analytic expressions in Eqs. (34) and (35). For field driven coherences, the analytic expressions require the evaluation of the first moments in Eqs. (A1)–(A2) and (A4) of Appendix A. The moments can be evaluated in a single step before doing the time integrals. Hence, two of the time integrations are eliminated and the overall computation time is significantly reduced. The signal amplitude and phase in either of these approaches are obtained by performing a Fourier transform of the delay dependent pump–probe signal in Eq. (18). An alternative method that can be used when vibrational damping is neglected, is to directly calculate the amplitude and phase of the dispersed and open band signals using the analytic expressions derived in Sec. III B 2. For calculations involving only a few modes, the analytic formula for the dispersed signal in Eq. (38b) can be easily evaluated, and a subsequent integration over frequencies as in Eq. (19) leads to the open band amplitude and phase.

In what follows, we demonstrate that amplitude and phase excitation profiles of field induced coherence are equally well-predicted by the third-order and the effective linear response approaches. We then apply the effective linear response approach to calculate coherent signals induced by rapid nonradiative reactions.

A. Temperature and carrier frequency dependence

One of the key parameters in a pump–probe experiment is the carrier frequency of the pump and probe laser pulses. Not only is this parameter the most easily accessible to the experimentalist, but measurements of the oscillatory amplitude and phase profiles through the resonant region provide crucial information regarding the origin of vibrational coherence.[11,15,35] The computational simplicity of the effective linear response approach, using the first moments, enables a direct calculation of phase and amplitude profiles over the entire absorption spectrum using realistic pulse widths.

In order to illustrate the accuracy and the physically intuitive aspects of the effective linear response approach, we treat a simple model system. Consider a single undamped mode with $\omega_0=40\,\mathrm{cm}^{-1}$ and $S=(\Delta^2/2)=0.5$ coupled to a homogeneously broadened two-level system with $\Gamma_e=800\,\mathrm{cm}^{-1}$. We assume 10 fs pump and probe pulses in a degenerate (same color for pump and probe) configuration. The short pulse width allows comparison with the third-order response calculation which is quite formidable for long pulse durations $\sim(50-100)$ fs. Expressing the delay dependent oscillatory signal as

$$S(\tau)=A_s\cos(\omega_0\tau+\phi_s), \tag{48}$$

we plot in Fig. 2 the degenerate open band amplitude A_s and the phase ϕ_s profiles for the $40\,\mathrm{cm}^{-1}$ oscillations. The ground and excited state profiles are plotted for a range of carrier frequencies across the absorption maximum. The top panels of Figs. 2(a) and 2(b) show the ground and excited state amplitude and phase profiles for $T=0$ K and $T=300$ K. Both the third-order response and the effective linear response outputs are plotted. The excellent agreement between the two approaches is evident over the entire range of carrier frequencies. We note that the ground and excited state amplitudes dip near the classical absorption and emission peaks, respectively, Ω_v and $\Omega_v-2\omega_0 S$. The phase of the ground state signal shows a variation of 2π as the carrier frequency is detuned across Ω_v. There is a sharp jump between $\pm(\pi/2)$ at Ω_v. In contrast to the ground state, the excited state phase remains constant apart from a π phase jump at $\Omega_v-2\omega_0 S$. At low temperature, the amplitude of the ground state signal drops by almost an order-of-magnitude. The approach of the phase toward $\pm(\pi/2)$ on either side of the discontinuity at Ω_v is steady and almost linear. For the high temperature case, the approach of the phase toward $\pm(\pi/2)$ occurs much more sharply near Ω_v. While the excited state phase is independent of temperature, the excited state amplitude becomes more asymmetric as the temperature is increased, as seen in Fig. 2(b).

All of the above aspects of the ground and excited state signals can be clearly understood using the first moments of the pump induced oscillations; see Appendix A. First, recall that the open band phase yields the initial phase of the pump induced oscillation to within an additive factor of π as in Eq. (44b). This is shown for the ground state signal in Fig. 3. We plot the open band phase of the $40\,\mathrm{cm}^{-1}$ mode over an expanded range that includes the off-resonant limit, along with the initial phase of the wave packet calculated using Eqs. (A1) and (A2). Figure 3(c) schematically depicts the effective initial conditions prepared by the pump pulse in the ground and excited states. Shown are the initial conditions for three different pump carrier frequencies, near resonance [indicated by downward pointing arrows in Fig. 3(a)] and off-resonance towards the red side of the absorption maximum. The arrows above the wave packets indicate the direction of the momentum induced by the pump pulse. From Eqs. (A1)–(A2), we note that the mean nuclear position and momentum in the ground state depend on the derivative of the absorption and dispersion line shapes, respectively.[47] Thus, the wave packet is undisplaced from equilibrium for excitation at $\omega_c=\Omega_v$. The momentum attains a maximum value at this frequency, and is signed opposite to the excited state equilibrium position shift.[47,45,44]

As depicted in Fig. 3, when the pump pulse carrier frequency is tuned toward the red side of the absorption maximum ω_R, the ground state wave packet is displaced toward decreased bond lengths and receives a momentum kick in the same direction. Thus, a probe pulse of carrier frequency ω_R incident on the sample sees an initially depleted nuclear distribution (bleach) in the ground state. The probe difference transmission signal (pump-on minus pump-off) will at $\tau=0$ be positive and will simultaneously have a positive slope due to the sign of the wave packet momentum. This is seen from the delay dependent signal plotted directly below the potentials in Fig. 3(c). The phase of the oscillatory signal $S(\tau)$ in Eq. (48) will obey $(3\pi/2)<\phi_s<2\pi$. On the other hand, for blue detuning from absorption maximum ω_B, the initial transmission signal will again be positive due to a depleted nuclear distribution in the probed region. However, the signal has a negative slope at $\tau=0$, since now the momentum of the wave packet points toward the probing region. In this case the signal phase will obey $0<\phi_s<(\pi/2)$ and is also precisely in phase with the wave packet itself. When the carrier frequency is tuned to resonance at ω_v, the pump pulse merely imparts a momentum to the wave packet so that the wave packet phase is precisely $(\pi/2)$. As described below, the CSRS and CARS resonances are oppositely phased for excitation at resonant maximum. The integrated signal therefore vanishes at ω_v and the phase becomes undefined. Incrementally to the red and blue sides of the absorption maximum, the open band phase shows a discontinuous jump of π since the momentum impulse always points in the same direction in the resonance region. Note that Fig. 3(c) shows, for ω_v, the oscillatory signal incrementally to the red of the absorption maximum, before the phase jump.

A similar analysis is possible for the excited state signal. The excited state response arises from the stimulated emission (by the probe) from the vibrationally coherent excited state. Since the excited state wave packet oscillates about the shifted equilibrium position Δ, the amplitude dip and phase

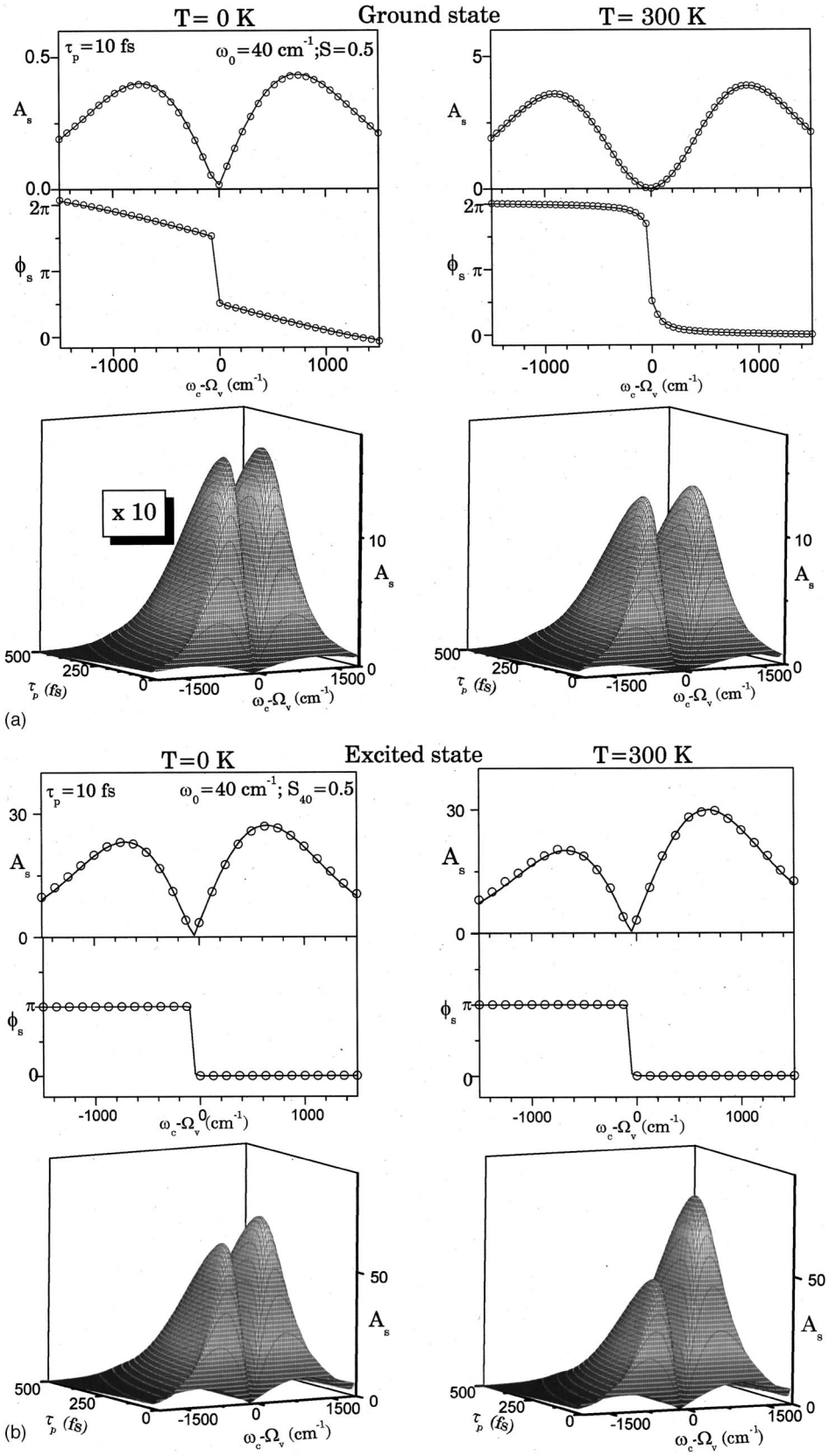

FIG. 2. Comparison of one-color pump–probe open band amplitude A_s and phase ϕ_s profiles predicted by the first moment based effective linear response approach (solid line) and the third-order response approach (circles). The profiles shown are for a single undamped mode ($\omega_0 = 40\ \mathrm{cm}^{-1}$, $S = 0.5$) coupled to a homogeneously broadened ($\Gamma_e = 800\ \mathrm{cm}^{-1}$) two-level system at $T = 300$ K and $T = 0$ K. The top panels of (a) and (b) show the amplitude and phase profiles for pulse width of 10 fs. The bottom panels of (a) and (b) show the amplitude of the ground and excited state signals as two-dimensional functions of the pulse width τ_p and the pulse carrier frequency ω_c, for both $T = 0$ K and $T = 300$ K. The analytic expressions in Eqs. (38)–(42) were employed in the 2D simulations.

flip of the pump–probe signal from the excited state occurs near the classical emission peak at $\Omega_v - 2\omega_0 S$. As depicted in Fig. 3(c), the excited state wave packet does not receive a momentum impulse; see Appendix A. Furthermore, it is created on the same side of the excited state harmonic well irrespective of the pump carrier frequency.[47] Thus, the phase of the excited state wave packet is independent of the pump carrier frequency. The corresponding signal phase is fixed at 0 for blue detuning where there is increased stimulated emission at $\tau = 0$. The phase is fixed at π for red detuning where

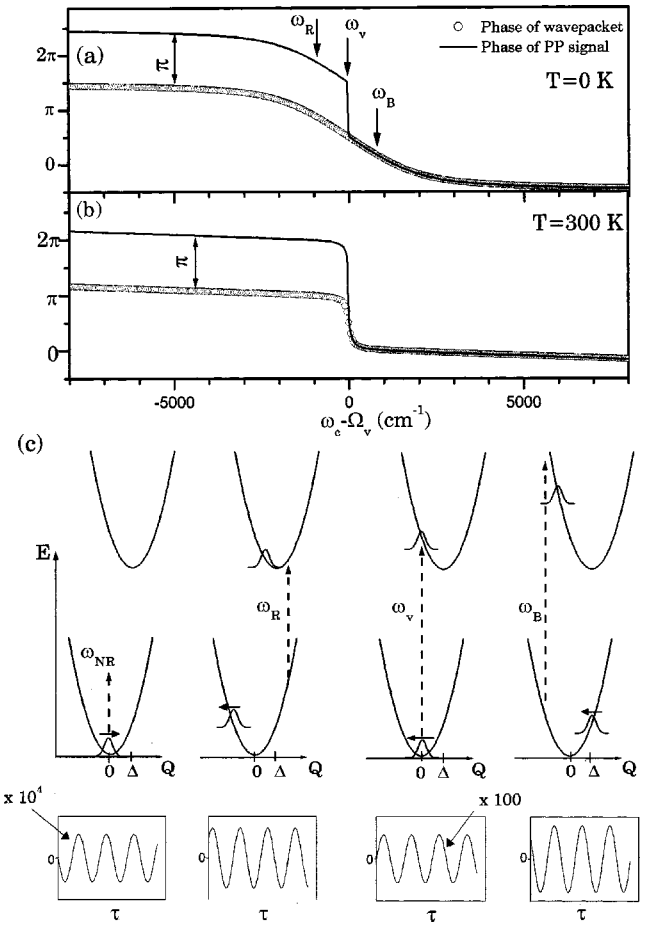

FIG. 3. Interpretation of the open band phase for the ground state signal in terms of the first moments of the pump induced nuclear wave packets. (a) The phase ϕ_s of the 40 cm^{-1} mode (from the example in Fig. 2) at $T=0$ K is plotted (solid line) along with the initial phase φ_g of the pump induced wave packet (circles). (b) Same as in (a) but for $T=300$ K. (c) Schematic of the pump induced effective initial conditions in the ground and excited states in a two-level system, shown for three different pump/probe carrier frequencies across the absorption maximum Ω_v, and for nonresonant excitation ω_{NR}. The arrows above the wave packets indicate the direction of the momentum imparted. The panels directly below the potential curves show the corresponding oscillatory signal as a function of pump–probe delay time.

the stimulated emission is minimum at $\tau=0$. Note in Fig. 2(b) the nearly order-of-magnitude increase in the amplitude of the excited state signal compared to the ground state. The increase can be traced to the fact that for impulsive excitation using weak fields, the excited state wave packet is situated very close to the vertical energy gap Ω_v. This corresponds to the ground state hole that has a displacement much smaller than Δ.[51,63,47] Thus, the amplitude of excited state oscillations about the equilibrium position Δ is much larger than that of ground state oscillations about zero. The excited state coherence will thereby be the dominant contribution for systems with long-lived excited states.[1,5–7,11,20] The asymmetry in the excited state amplitude profile can be seen in Fig. 3(c) to arise from the fact that the wave packet amplitude in the excited state is larger for blue excitation than for red.[47]

The temperature dependence of the oscillatory amplitude and phase in Fig. 2 can be understood via the relative temperature dependence of the initial position and momentum induced by the pump pulse. For high temperatures, the mean thermal phonon population $\bar{n}\gg 1$ and Q_{g0} is enhanced according to Eq. (A1), so that the complex displacement $\lambda_g=(Q_{g0}+iP_{g0})/\sqrt{2}$ is dominated by the real part. Hence the initial phase of the wave packet stays closer to zero or π at higher temperatures, except near Ω_v, where Q_{g0} vanishes. Correspondingly, the open band phase also stays closer to zero (or 2π) except for the discontinuous transition near Ω_v. When the temperature is lowered, Q_{g0} drops sharply since $\bar{n}\ll 1$ and becomes comparable in magnitude to P_{g0}. Thus, at low temperatures, the amplitude of the ground state signal drops dramatically, and the phase varies almost linearly on either side of the discontinuity at Ω_v as in Fig. 2(a). The temperature dependence of the excited state first moment Q_{e0} is primarily determined by the relative magnitude of $\Phi_I(\omega)$ and the difference line shape $\hat{\Delta}\Phi_I(\omega)$, which appears as the coefficient of $\bar{n}$ in Eq. (A4). The difference line shape is responsible for enhancing the asymmetry in the amplitude profile at high temperatures as in Fig. 2(b).

An important observation to be made from Fig. 3(c) is that for the linearly displaced oscillator model, the amplitude and phase profiles of field driven coherence are independent of the sign of the electron nuclear coupling Δ. If Δ were negative, then the same arguments given above would apply. The amplitude and phase behavior would be the same as in Fig. 2. This can be seen directly from the fact that the nonlinear response functions in Eqs. (C2a)–(C2b) and (C5a)–(C5b) depend only on Δ^2 through the function $g(s)$. However, the schematic depicted in Fig. 3 clearly indicates that the absolute sign of the potential displacements are not revealed in a pump–probe experiment.

The depiction of pump induced initial conditions in Fig. 3 contradicts prior predictions arising from time dependent wave packet pictures of impulsive stimulated light scattering.[64,8,65] The prior work suggests that the ground state wave packet is always created on the side of the ground state well that is closer to the excited potential minimum. This is not correct, as is shown by a careful analysis of the pump pulse interaction.[47,46,45] It is clear from Fig. 3(c) that the centroid of the ground state wave packet induced by impulsive excitation is strongly sensitive to the carrier frequency of the laser pulse.

From Figs. 2(a) and 2(b) we conclude that the moment analysis-based approach offers a physically intuitive and accurate interpretation of the observed amplitude and phase behavior of open band FCS signals. Another significant advantage offered by this approach is that the analytic form of the effective linear response functions reduces the computation times. For the comparisons made in Figs. 2 and 3 (top panels), we chose a very short 10 fs pulse in order to make the calculations using the third-order approach possible with reasonable computation times. However, in many experimental situations, including those reported here, the pulse width is often much longer ($\sim$100 fs). For long pulse widths the two extra integrations involved in the third-order approach makes the computation quite formidable. In Fig. 4, we compare the computation times for the linear response and third-order response calculations as a function of pulse width τ_p. The advantage offered by the effective linear re-

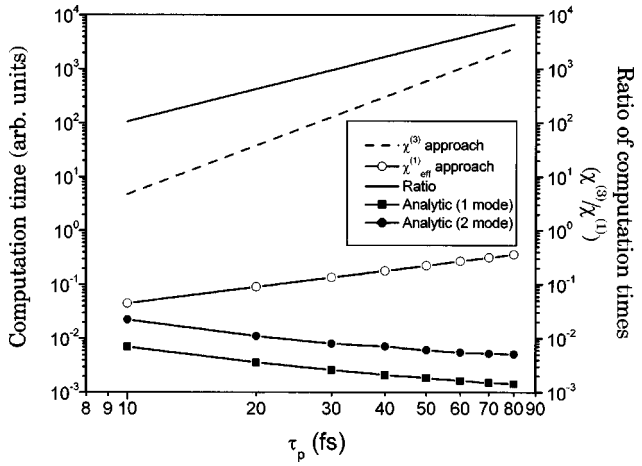

FIG. 4. Comparison of computation times for the calculation of the one-color ground state pump–probe signal, using the third-order response approach and the effective linear response approach, as a function of pulse width. Both the absolute time to calculate the signal for $40\omega_c$ points and the ratio of the computation times for the two approaches are plotted. Also shown is the computation time for calculating the profiles using the analytic expressions for the pump–probe signal in Eqs. (38)–(42).

sponse approach is clear, especially when it is of interest to calculate the amplitude and phase profiles at many carrier frequencies. The computation time for calculating the open band amplitude and phase using the analytic formulas in Eqs. (38)–(42) for a single mode and a two-mode case is also plotted in the figure. The integral of the analytic expressions is over the spectral profiles of the probe pulse so that a larger value of τ_p implies a narrower range of integration. In contrast to the numerical integrations in time domain, the computation time in this case therefore decreases with τ_p. As the number of modes involved increases, the summation in Eq. (38b) involves multiple indices and the calculation becomes more complex. However, the usefulness of the analytic expression for a few modes is evident from Fig. 4.

As an illustration of the use of the analytic expressions, we calculate the ground and excited state amplitude profiles for a wider range of pulse widths (5 − 500) fs in the bottom panels of Figs. 2(a) and 2(b). The three-dimensional plots are useful in capturing the behavior of pump–probe signals over a wide range of pulse widths and carrier frequencies. It is seen that the temperature dependence of the ground state signal amplitude is rather uniform over the entire manifold of τ_p and ω_c. The excited state signal shows more interesting behavior, with the asymmetry in the amplitude profiles more pronounced at longer pulse widths. Both the ground and excited state amplitudes vanish in the limit of very short and very long (compared to the vibrational period) pulses, attaining an optimum for some intermediate value of τ_p. The vanishing of the ground state signal for $\tau_p \to 0$ can be traced to the fact that the ground coherence vanishes in the short pulse limit.[44,8,27,47] It is interesting to note from Eq. (A4) that the excited state nuclei are however coherent for $\tau_p \to 0$. It can be shown that the corresponding density matrix is simply thermal density matrix $\hat{\rho}_T^{(e)}$ placed vertically above $Q=0$ on the excited state potential well.[47] Note that the representation in Eq. (13) is essentially exact in this limit. The vanishing of the excited state open band signal for $\tau_p \to 0$ occurs rather due to the fact that the open band signal for a spectrally broad probe is essentially the integral over the derivative-like basis functions, $\Theta_{I,R}^{(k)}(\omega)$, which are analogous to $\Phi_{I,R}^{(k)}(\omega)$ plotted in Fig. 5 (see below).

Finally, we consider a two-color pump–probe experiment, which employs a fixed carrier frequency for the pump and a variable carrier frequency of the probe. The analysis presented so far applies equally well to two-color pump–probe experiments. In this case, the pump imparts a fixed

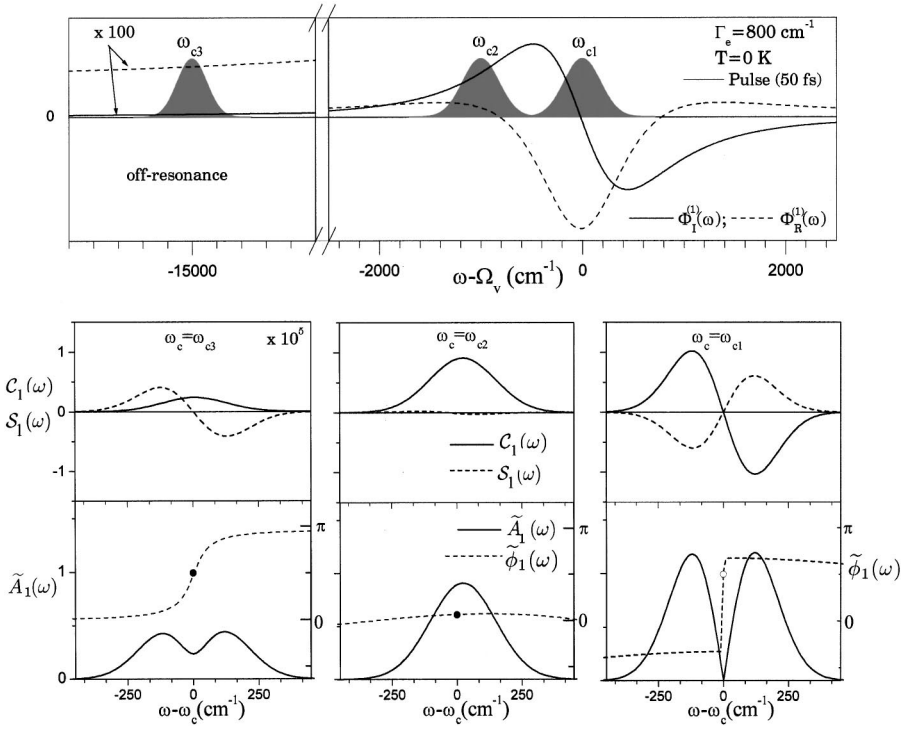

FIG. 5. Dispersed pump–probe signal for the two-electronic level system considered in Fig. 2. The top panel shows the absorptive and dispersive basis functions $\Phi_I^{(1)}(\omega)$ and $\Phi_R^{(1)}(\omega)$ defined in Eqs. (42a) and (42b), for $T=0$ K. The spectral profile of the pulse ($\tau_p=50$ fs) is shown for three different pulse carrier frequencies. The bottom panels show the corresponding quadrature amplitudes $\mathcal{C}_1(\omega)$ and $\mathcal{S}_1(\omega)$, and the amplitude $\tilde{A}_1(\omega)$ and phase $\tilde{\phi}_1(\omega)$ of the 40 cm^{-1} fundamental of the dispersed signal. The open band phase for each carrier frequency is also shown (filled circle).

initial condition to the wave packet that is determined from the results of Appendix A. The signal amplitude and phase profiles as a function of the probe carrier frequency will be similar to that of the excited state degenerate pump–probe signal. The amplitude will exhibit a dip at Ω_v, and the signal phase will be the initial wave packet phase, but for a π jump at Ω_v. Since the pump induced initial conditions are independent of the probe carrier frequency ω_c, the computation of two-color pump–probe profiles is less cumbersome than the degenerate pump–probe profiles.

B. Dispersed pump–probe measurements and off-resonant response

When the pump pulse is tuned off-resonance, $\hat{\Delta}\Phi_I(\omega) \rightarrow 0$ and Eqs. (A1)–(A2) show that the ground state wave packet merely receives a momentum kick, and is undisplaced from its equilibrium position. Thus, the phase of the open band signal approaches $\pm(\pi/2)$ as seen from Figs. 3(a) and 3(b). Furthermore, the dependence of the wave packet momentum on $\hat{\Delta}\Phi_R$ implies that the momentum impulse changes direction as we begin to move off-resonance on the red and blue sides of the absorption maximum. Correspondingly, the signal phase crosses 2π (zero) into the first (fourth) quadrant as seen in Figs. 3(a) and 3(b). The approach of the open band phase toward the off-resonant limit of $\pm(\pi/2)$ is more dramatic at lower temperatures, where P_{g0} is comparable in magnitude to Q_{g0}. At high temperatures, the magnitude of Q_{g0} is dramatically enhanced relative that of P_{g0} because of the thermal factor in Eq. (A1). This enhances the contribution of $\hat{\Delta}\Phi_I(\omega)$ to the signal phase. The off-resonant limit is thus attained at further detuning from absorption maximum at high temperatures.

While the open band (dichroic) signal approaches zero off-resonance, we showed earlier that the dispersed probe signal does not vanish in this limit and is related to $\Phi_R(\omega)$ as in Eq. (45). In Fig. 5, we demonstrate the on- and off-resonance behavior of the dispersed signal, using the same model parameters as in Fig. 2. In the top panel, we plot the basis functions for the $T=0$ ground state fundamental ($k=1$) oscillations $\Phi_I^{(1)}(\omega)$ and $\Phi_R^{(1)}(\omega)$ given by Eqs. (42a)–(42b). The basis functions for $k=1$ are seen to behave roughly as the first derivatives of the absorption and dispersion lineshapes. Similarly, the basis functions for the first overtone $\Phi_I^{(2)}(\omega)$ and $\Phi_R^{(2)}(\omega)$ can be shown to behave like the second derivatives of the line shapes and so on. The Gaussian spectral profile of the laser pulse ($\tau_p=50$ fs) used in the calculation is also shown in the upper panel for three different carrier frequencies ω_{c1}, ω_{c2}, and ω_{c3}. The functions $\mathcal{C}_1(\omega)$ and $\mathcal{S}_1(\omega)$ and the dispersed probe amplitude and phase $\tilde{A}_1(\omega)$ and $\tilde{\phi}_1(\omega)$ are plotted directly below. As specified in Eqs. (40a) and (40b), the quadrature amplitudes $\mathcal{C}_1(\omega)$ and $\mathcal{S}_1(\omega)$ are obtained by superposing the Stokes and anti-Stokes shifted product functions $G_p(\omega_d, \omega_0)\Phi_{I,R}^{(1)}(\omega)$ and $G_p(\omega_d, -\omega_0)\Phi_{I,R}^{(-1)}(\omega)$, which correspond to CSRS and CARS resonances, respectively. While the (dichroic) Stokes and anti-Stokes components are additive for $\mathcal{C}_1(\omega)$ they are subtractive for $\mathcal{S}_1(\omega)$. It is clear from Fig. 5 that at the absorption maximum $\omega_c=\omega_{c1}$, the derivative nature of $\Phi_I^{(1)}(\omega)$ gives rise to Stokes and anti-Stokes components of $\mathcal{C}_1(\omega)$ that are oppositely signed on either side of the carrier frequency. Thus, the dispersed signal is π out of phase for red and blue detuning from the carrier frequency. The integral of both $\mathcal{C}_1(\omega)$ and $\mathcal{S}_1(\omega)$ vanishes, giving rise to a dip in the open band signal amplitude. When the carrier frequency is tuned near the shoulder of the absorption spectrum $\omega_c=\omega_{c2}$, the Stokes and anti-Stokes components of $\mathcal{C}_1(\omega)$ add constructively to give a single peak. $\mathcal{S}_1(\omega)$ is very small compared to $\mathcal{C}_1(\omega)$ since $\Phi_R^{(\pm 1)}(\omega)$ are small in this region. For off-resonant excitation $\omega_c=\omega_{c3}$, the dispersive term $\mathcal{S}_1(\omega)$ begins to dominate and the signal approaches the limit in Eq. (45). While the details of the behavior of the dispersed probe signal are highly mode specific,[66] the simulations shown in Fig. 5 illustrate the general aspects of the dispersed pump–probe signals based on equilibrium line shape functions.

It is clear from Fig. 5 that the direct connection with equilibrium line shapes made in Eqs. (38)–(42) allows a clear picture of the dispersed probe measurements. Furthermore, when dealing with complex multimode systems, one can directly use the experimentally measured absorption line shape and its Kramers–Kronig transform, the dispersive line shape. The need for modeling the detailed mechanisms responsible for line broadening is thus avoided. However, additional steps are required when inhomogeneous broadening is significant (see below). Generally, this approach is analogous[67] to the use of transform methods in the calculation of resonance Raman scattering cross sections.[68–70,56]

C. Effects of inhomogeneous broadening

Until now, we have assumed that the molecular system under consideration has a fixed electronic energy gap (Ω_{00}) and a homogeneously broadened absorption spectrum. The homogeneous broadening mechanism reflects the electronic population decay as well as the rapid fluctuations that take place between the system and the environment. In addition to the homogeneous contribution, the width of the absorption line shape can also have a quasistatic origin. For example, a distribution of electronic transition frequencies arising from local changes in the environment or disorder in the system.[71] Several spectroscopic techniques exist,[72–74] which can be used to selectively probe the effects of inhomogeneous broadening. In this section, we consider the effects of inhomogeneous broadening on pump–probe signals. Experimental examples of open band phase measurements on myoglobin (Mb) are presented to demonstrate the presence of an asymmetric inhomogeneously broadened absorption spectrum for Mb.

In the presence of inhomogeneous broadening, the homogeneous pump–probe signal must be averaged over the inhomogeneous distribution $\mathcal{F}_I(\Omega_{00})$. In the third-order response approach, this averaging is simply a Fourier transform of the function $\mathcal{F}_I$ and can be carried out independently of the time integrations over the pump fields;[28] see Eqs. (C8a) and (C8b) of Appendix C. In the effective linear response approach, however, the averaging over $\mathcal{F}_I(\Omega_{00})$ cannot be carried out as in Eqs. (C8a) and (C8b). The time

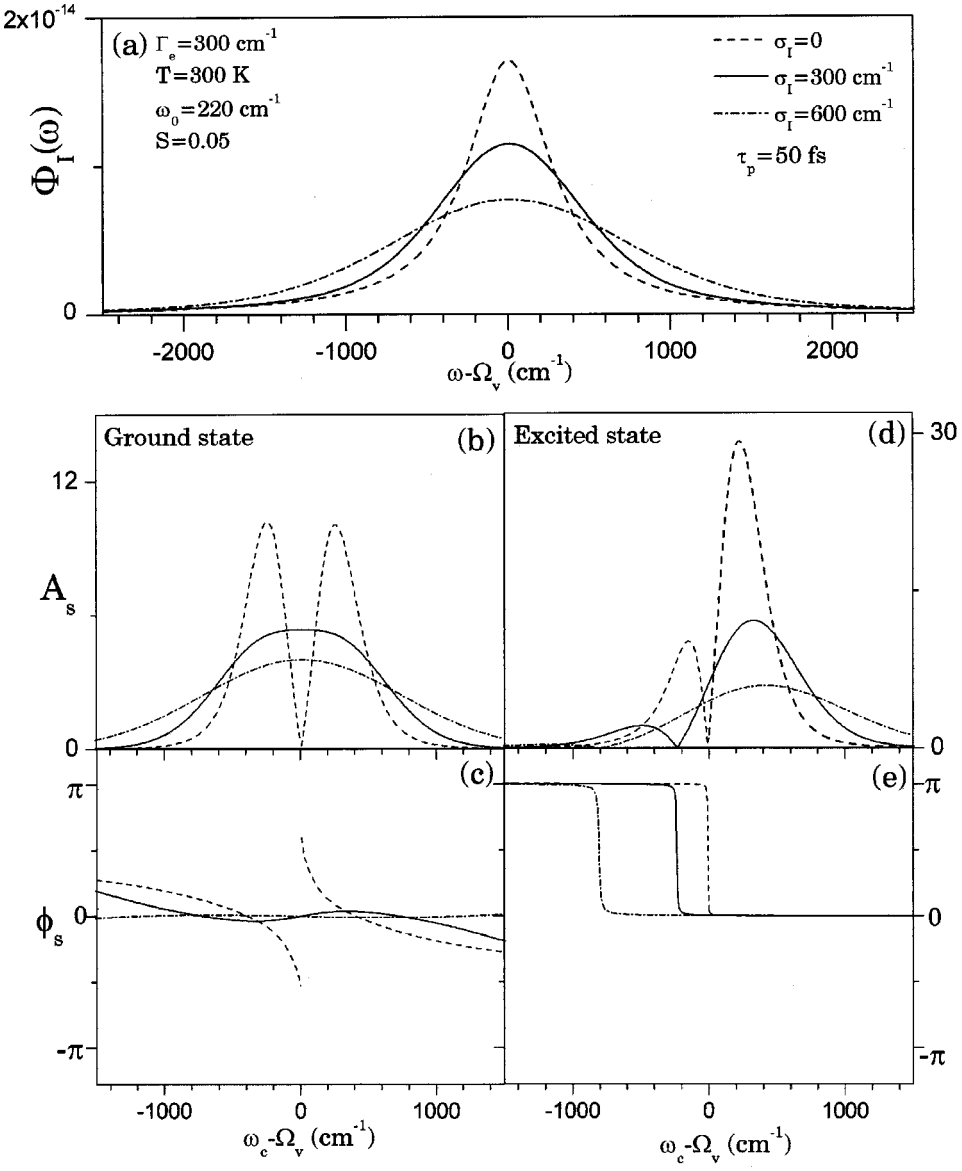

FIG. 6. Effects of inhomogeneous brodening on one-color pump–probe amplitude and phase profiles. (a) Shows the absorption line shape function for the homogeneous case (dashed line), and with Gaussian inhomogeneities of $\sigma_I = 300\,\mathrm{cm}^{-1}$ (solid line) and $\sigma_I = 600\,\mathrm{cm}^{-1}$ (dash-dot line). The amplitude and phase profiles for the ground state case are shown in panels (b) and (c), for the three line shapes. The corresponding excited state amplitude and phase are shown in panels (d) and (e).

integrations over t_1 and t_2 involved in the pump interaction are carried out separately to find the first moments. Ω_{00} appears through the line shape functions $\Phi_I(\omega)$ and $\Phi_R(\omega)$ in the first moment expressions, Eqs. (A1)–(A2). In order to include the inhomogeneities, we first calculate the homogeneous pump–probe signal and then numerically average the signal over the distribution $\mathcal{F}_I(\Omega_{00})$. When experimentally measured line shapes are used in place of the time correlator expressions, the homogeneous line shape must be deconvolved from the measured line shapes before being used in the pump and probe steps of the calculation. The inhomogeneous pump–probe signal is obtained by a final convolution of the homogeneous pump–probe signal with the inhomogeneous distribution.

Inhomogeneous broadening affects the ground and excited state responses in a distinct fashion, owing to their contrasting phase behavior. Recall that the ground state signal is approximately in phase on either side of the resonant maximum Ω_v. Since the inhomogeneous pump–probe signal is essentially a superposition of homogeneous signals, the inhomogeneous amplitude will be nonvanishing at Ω_v. The phase discontinuity will also be smeared out in the presence of inhomogeneity. In Fig. 6, we consider a homogeneous line shape with $\Gamma_e = 300\,\mathrm{cm}^{-1}$ and a single undamped $220\,\mathrm{cm}^{-1}$ mode with coupling $S = 0.05$. Pump–probe signals are calculated for $T = 300\,\mathrm{K}$ using both the homogeneous line shape and with Gaussian inhomogeneities included. The top panel in the Fig. 6 shows $\Phi_I(\omega)$ with three values of the inhomogeneous width $\sigma_I = 0$, 300, and $600\,\mathrm{cm}^{-1}$. The lower panels show the amplitude and phase of ground and excited state signals for the three cases assuming a pulse width of $\tau_p = 50\,\mathrm{fs}$.

It is seen that while the amplitude dip and phase discontinuity of the ground state signal are dramatically removed by the inhomogeneity, they exhibit a red-shift for the excited state. The shift of the excited state signal arises from the asymmetry of the excited state amplitude: since the amplitude of the homogeneous stimulated emission signal on the red side is much smaller than on the blue side of Ω_v, an effective cancellation of the positive and negative lobes of the signed amplitude will occur towards the red.

Example: Inhomogeneous broadening in myoglobin

The characteristic features of the ground and excited state amplitude and phase profiles can be used as indications of inhomogeneous broadening. As an example, consider the heme protein deoxy myoglobin (Mb), which is an oxygen storage protein found in muscle cells. Mb possesses a highly asymmetric and broad absorption spectrum (Soret band) in its ligand-free, high spin (deoxy, $S=2$) state. In previous studies, the Soret band of Mb was modeled using a non-Gaussian distribution of electronic energy levels, ascribed to disorder in the position of the central iron atom of the porphyrin ring.[71,75] In pump–probe and resonance Raman experiments on Mb, the Soret excited state is found[76,35] to be very short lived ($\leqslant 30$ fs). Thus, the detected pump–probe signals for deoxy Mb are presumably due to ground state coherence driven by impulsive stimulated Raman scattering. Here, we focus attention on the Fe–His mode at $220\,\mathrm{cm}^{-1}$ which is a prominent mode in the resonance Raman experiments on Mb.

In the top panel of Fig. 7, we plot the experimental absorption spectrum of Mb along with a theoretical fit based on the previously proposed model for the inhomogeneous distribution.[71,75] All resonance Raman active modes are included in the model, with coupling strengths determined from their absolute resonance Raman cross sections.[77] The pump–probe calculations are carried out using the effective linear response approach using a realistic pulse width of 70 fs. For simplicity, only the $220\,\mathrm{cm}^{-1}$ mode ($S=0.05$) was taken to be displaced from equilibrium. In Fig. 7(b), we plot the phase profile of the $220\,\mathrm{cm}^{-1}$ mode observed in open band (one color) pump–probe measurements on Mb across the absorption maximum. The theoretical prediction for the phase of the $220\,\mathrm{cm}^{-1}$ mode in the ground state is shown for both the inhomogeneous line shape model[71,75] as well as for a homogeneous model that fits the observed line shape.

It is clear from Fig. 7(b) that the theoretical prediction using the inhomogeneous line shape is in good agreement with the experimental data. Note that the phase approaches the off-resonant limit of $(\pi/2)$ much more rapidly on the red side than on the blue side of the absorption maximum. This reflects the strong asymmetry in the absorption spectrum. The sharp phase jump between $-(\pi/2)$ to $+(\pi/2)$ predicted by the homogeneous model is clearly not observed in the experimental data. Also, the amplitude of the $220\,\mathrm{cm}^{-1}$ mode does not show a clear dip near absorption maximum, contrary to the prediction of the homogeneous model. These observations strongly support the presence of significant inhomogeneous broadening in deoxy Mb, as well as the ground state origin of the vibrational oscillations. If the $220\,\mathrm{cm}^{-1}$ coherence originated from the excited state rather than the ground state, an amplitude dip and phase flip should be observed but red-shifted from the emission maximum as discussed above.

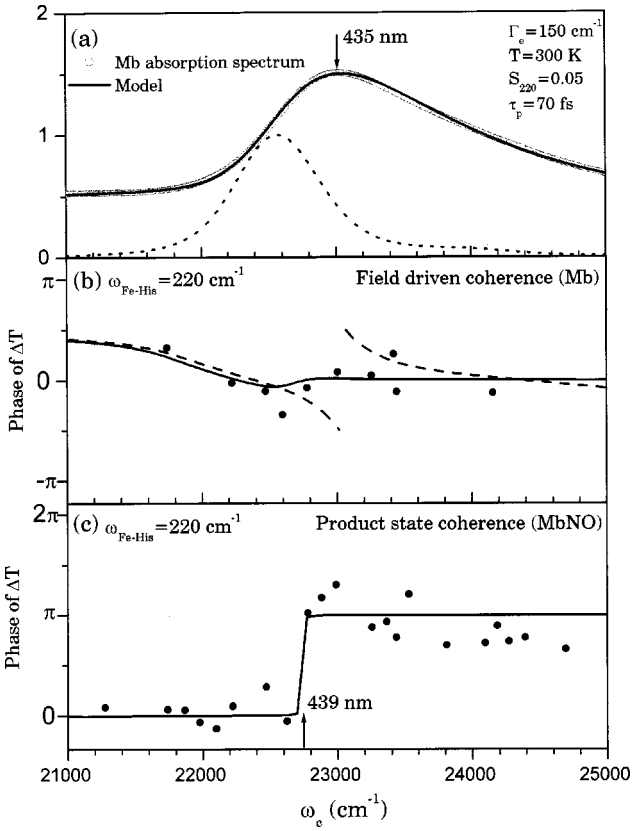

FIG. 7. (a) Equilibrium absorption spectrum of Mb at $T=300$ K (open circle) shown with the theoretical fit (solid line) based on a prior model for the asymmetric deoxy Mb line shape. The underlying homogeneous line shape (before convolution with inhomogeneities) is also shown (dotted line). (b) Experimental Soret band phase profile for $220\,\mathrm{cm}^{-1}$ mode coherence from deoxy Mb (filled circles) is shown with the theoretical fit based on an inhomogeneous model (solid line) and a homogeneous model (dashed line) using the asymmetric line shape plotted in (a). (c) Experimental phase profile for the $220\,\mathrm{cm}^{-1}$ mode in MbNO for a range of carrier frequencies across the Soret band is shown with a theoretical fit based on simple model for reaction driven coherence in MbNO.

D. Reaction driven coherence: Coherent oscillations in MbNO

We now apply the effective linear response approach to coherence driven by a chemical reaction of the type shown in Fig. 1(b). The effective linear response function for a two-level system consisting of the product ground and excited states $|f\rangle$ and $|f'\rangle$ was discussed in Sec. III B 3. The nuclear density matrix for the state $|f\rangle$ is described by a displaced thermal density matrix. The displacements are the first moments of the vibrational coherence driven by a Landau–Zener surface crossing between the nonradiative states $|e\rangle$ and $|f\rangle$ presented in Appendix B. The pump–probe signal arises from the vibrationally coherent state $|f\rangle$. As discussed earlier, we are concerned with the situation where the vibrational mode Q is not coupled to the $g\rightarrow e$ optical excitation, but is triggered solely by the nonradiative chemical reaction between $|e\rangle$ and $|f\rangle$ that follows pump excitation. For example, Q could represent the $220\,\mathrm{cm}^{-1}$ Fe–His mode in the reactive sample MbNO. The $220\,\mathrm{cm}^{-1}$ mode is not resonance Raman active in the reactant ground state ($|g\rangle$) but is nevertheless observed in pump–probe photolysis signals.

The spectral line shape function also plays an important role in the multidimensional Landau–Zener theory.[21] As specified in Eq. (B2) of Appendix B, the transition rate between the states $|e\rangle$ and $|f\rangle$ is obtained by taking the zero frequency limit of the spectral function for the $e\rightarrow f$ transi-

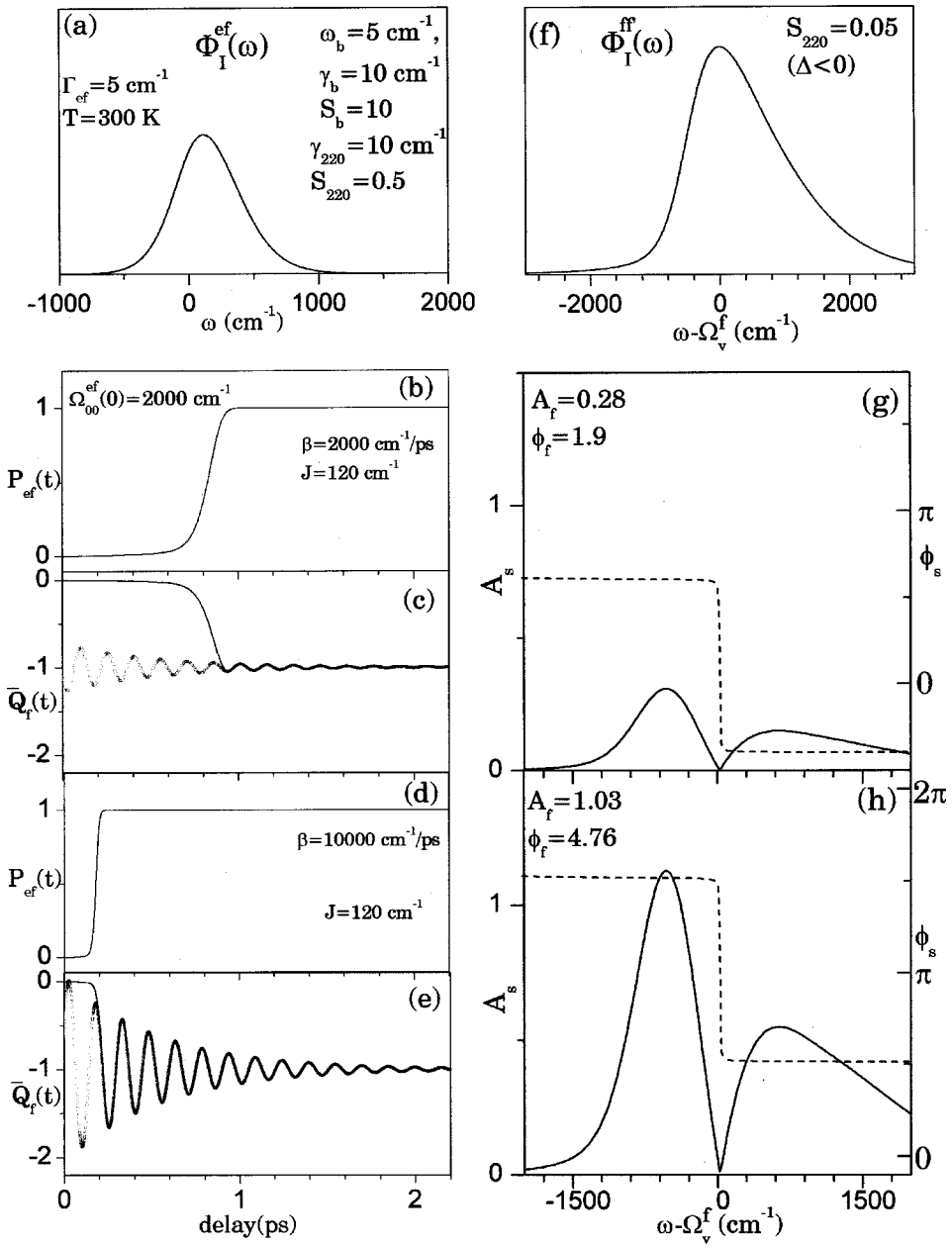

FIG. 8. Application of the effective linear response approach to reaction driven coherence. (a) Spectral line-shape function for the nonradiative $e \rightarrow f$ electronic transition. Panels (b) and (d) show the time-dependent population evolution of the product state for reaction velocities of $\beta = 2000\ \mathrm{cm}^{-1}/\mathrm{ps}$ and $\beta = 10\,000\ \mathrm{cm}^{-1}/\mathrm{ps}$. Panels (c) and (e) show the corresponding mean position of the $220\ \mathrm{cm}^{-1}$ mode coupled to the reaction. The calculations using the effective initial conditions, Eqs. (B4)–(B6), are shown in circles. The results of a direct integration as in Eq. (B3) are shown as a solid line. The nonradiative coupling strength was fixed at $J = 120\ \mathrm{cm}^{-1}$ in both the calculations. (f) Spectral line shape function for the product state [identical to the Mb line-shape in Fig. 7(a)]. (g) and (h) show the pump–probe open band amplitude A_s (solid line) and phase ϕ_s (dashed line) profiles arising from the reaction driven $220\ \mathrm{cm}^{-1}$ coherence in the product state, for $\beta = 2000\ \mathrm{cm}^{-1}/\mathrm{ps}$ and $\beta = 10\,000\ \mathrm{cm}^{-1}/\mathrm{ps}$.

tion i.e., $\Phi_I^{ef}(\omega=0,\Omega_{00}^{ef}(R(s)))$. Here, $\Omega_{00}^{ef}(R(s))$ is the time-dependent energy gap between the $|e\rangle$ and $|f\rangle$ states as shown in Fig. 1(b) and $R(s)$ is the time-dependent semiclassical reaction coordinate. As the reaction coordinate sweeps through the crossing point, $\Omega_{00}^{ef}(R(s))$ passes through zero. The reaction rate $\mathcal{G}(R(s))$ is integrated as in Eq. (B1) to obtain the time-dependent quantum yield $P_{ef}(t)$. In the present discussion, we hold to the assumption of constant reaction velocity at the crossing point. This means that the energy gap $\Omega_{00}^{ef}(R(s))$ is decreasing at a constant rate β.

Our aim here is to illustrate the analysis of pump–probe signals associated with the reaction dynamics, and we restrict our attention to the role played by the reaction velocity β. We refer the reader to Ref. 21 for the details of the role played by the various reaction specific parameters in the population and coherence dynamics. In Fig. 8(a), we simulate the spectral function Φ_I^{ef} for the nonradiative states. The coupling of the $220\ \mathrm{cm}^{-1}$ mode is taken as $S=0.5$ corresponding to the 0.1 Å Fe–His bond length contraction associated with the loss of the NO ligand. An over damped low frequency bath mode is also included to broaden the spectral function. In the panels directly below the line shape, the time-dependent population transfer $P_{ef}(t)$ and the first moment dynamics $\bar{Q}_f(t)$ in the product state are plotted. $\bar{Q}_f(t)$ is obtained both by direct integration using Eq. (B3) and the initial first moments using Eqs. (B4)–(B6). A reaction velocity of $\beta = 2000\ \mathrm{cm}^{-1}/\mathrm{ps}$ and $\beta = 10000\ \mathrm{cm}^{-1}/\mathrm{ps}$ are considered in Figs. 8(b)–8(e). The initial vertical energy, corresponding to the separation of the quintet and singlet energy levels in MbNO, is taken to be $\Omega_{00}^{ef}(0) = 2000\ \mathrm{cm}^{-1}$. The connection between the time-dependent population evolution and the first moment dynamics in the product state is clearly exposed in the simulations. We see that for smaller β, the reaction proceeds in a smooth fashion, with a complete transition to the product occurring immediately after $t=1$ ps.

The slow passage through the reaction vertex causes the product state oscillations to be effectively diminished. For large β, the product electronic state population changes more abruptly, and the initial amplitude of the oscillatory motion is considerably larger, approaching the equilibrium displacement of the reactant well with respect to the product ($|\Delta_{ef}|=1$).

In Figs. 8(g)–8(h), we simulate the amplitude and phase profiles of the pump–probe signals associated with the reaction driven oscillations in the electronic state $|f\rangle$, using the inhomogeneous equilibrium line shape of Mb shown in Fig. 8(f). Note that only the product state electronic transition $f \rightarrow f'$ is inhomogeneosly distributed. The probe pulse detects the modulation of the $f \rightarrow f'$ electronic transition by the reaction driven oscillations. Since the initial conditions of the wave packet on the state $|f\rangle$ are independent of the pump wavelength, a sharp jump in the phase is observed accompanied by a dip in the amplitude at the absorption maximum Ω_v^f. The direct correspondence between the amplitude of the vibrational oscillations and the amplitude of the signal is evident from the simulations. The slower reaction exhibits a much weaker signal amplitude than the faster reaction. The signal phase directly yields the initial phase φ_f of the wave packet according to Eq. (44b). Furthermore, if we let $\gamma=0$ and $\dot{P}_{ef}(t)=\delta(t-\tau_R)$ in Eqs. (B5) and (B6), we have $\varphi_f \cong -\omega_0\tau_R$, $\tau_R=\Omega_{00}^{ef}(0)/\beta$ being the reaction time. Thus, when β is increased, τ_R decreases and the initial phase continually changes through cycles of 2π. The phase approaches zero for an infinitely fast reaction. It is interesting to note from Figs. 8(c) and 8(e) that the effective initial momentum of the wave packet (due to a nonzero φ_f) reverses its sign as β is increased from 2000 to 10 000 cm^{-1}/ps. Compare Fig. 3(c), where the momentum impulse has the same direction across resonance.

As an example, we consider the Fe–His mode in the reactive sample MbNO in Fig. 7(c). In contrast to the nonreactive Mb, the phase of the 220 cm^{-1} oscillation in MbNO exhibits a sharp jump at a wavelength that is red-shifted with respect to the Soret absorption maximum at $\sim$23 000 cm^{-1} (435 nm) of the Mb product. Also, the amplitude of the 220 cm^{-1} oscillations vanishes at this detection wavelength.[35] These observations are consistent with the suggestion that the Fe–His mode is driven by the chemical reaction associated with the $e \rightarrow f$ electronic transition as described in Fig. 8. The 4 nm red-shift of the phase flip is probably associated with the initial red-shift of the photoproduct absorption band[35] centered roughly at 439 nm ($\sim$22 780 cm^{-1}). The fact that the phase flip occurs precisely at this wavelength is consistent with the idea that the 220 cm^{-1} oscillations in MbNO are associated with the initial Mb photoproduct that is created following photodissociation of the NO ligand.

It is also seen from Fig. 7(c) that the phase of the open band 220 cm^{-1} oscillations is near 0 or π. This suggests that the initial phase of the 220 cm^{-1} mode coherence is also close to 0. A zero initial wave packet phase is realized if the reaction time τ_R is a small fraction of the 150 fs oscillatory period. The wave packet is then placed almost instantly ($\lesssim$20 fs) on the product state potential surface. In the Landau–Zener theory, the reaction time depends both on the reaction velocity β and on the initial vertical energy gap $\Omega_{00}^{ef}(R(0))$, suggesting that either the gap is small or the velocity is large (or both) in the MbNO reaction. As discussed earlier, this corresponds to a population evolution that behaves like a step function.

On the other hand, a zero initial phase of the wave packet could also be an indication of direct pump pulse preparation of the product state coherence. For example, when $\Omega_{00}^{ef}(R(0))$ is very small, the pump pulse interaction may directly excite an adiabatic mixture of the $|e\rangle$ and the $|f\rangle$ electronic states. The coherence induced along the Q coordinate will then have a phase of zero (no initial momentum), since it originated from the excited state directly prepared by the pump pulse. This possibility is beyond the scope of the present treatment, which assumes that the pump pulse and chemical reaction can be separated. We will address this interesting question in future work.

Finally, we point out that the absolute phase of the 220 cm^{-1} mode in MbNO indicates that the Fe–His bond in Mb ($|f\rangle$) contracts upon optical excitation to Mb* ($|f'\rangle$), as depicted in Fig. 1(b). This is based on the knowledge that the Fe–His bond also contracts upon loss of the NO ligand; i.e., upon the nonradiative transition between $|e\rangle$ and $|f\rangle$. The wave packet induced in $|f\rangle$ is therefore placed at positive displacements with respect to the equilibrium position. It is clear from Fig. 1(b) that if the Fe–His bond expands upon photoexcitation to $|f'\rangle$, exactly the opposite phase behavior from that observed in Fig. 7(c) would be predicted. This confirms earlier predictions[78] and also demonstrates that the phase of reaction driven pump–probe signals can provide information on the sign of the optical electron nuclear coupling, provided the initial ground state equilibrium changes are known.

E. Overtone signals

1. First moment modulation (coherent state)

Up to this point, we have focused on the oscillatory pump–probe signal at the fundamental frequency of the optically coupled mode. The presence of higher overtones is expected even for harmonic modes, since the observed signal is not directly the mean nuclear position oscillating at the fundamental frequency. The pump–probe signal arises from a dynamic modulation of the equilibrium correlator as expressed in Eqs. (34) and (35). Intuitively, if we picture a two-electronic level system, the overtone signal can be attributed to the ''double pass'' of the wave packet across the probing region.[11,44] The strength of the overtone signals due to the double pass is determined by the higher powers of the product $A_g\Delta$. This can been seen by expanding the exponential in the correlation function in Eq. (33). For weak field intensities, the pump induced ground state amplitudes are much smaller than the optical coupling strengths,[51,63,47] which are often much less than unity in large multimode systems. Thus, the overtones generated by the first moment modulation of the pump induced ground state wave packet are much weaker than the fundamental.

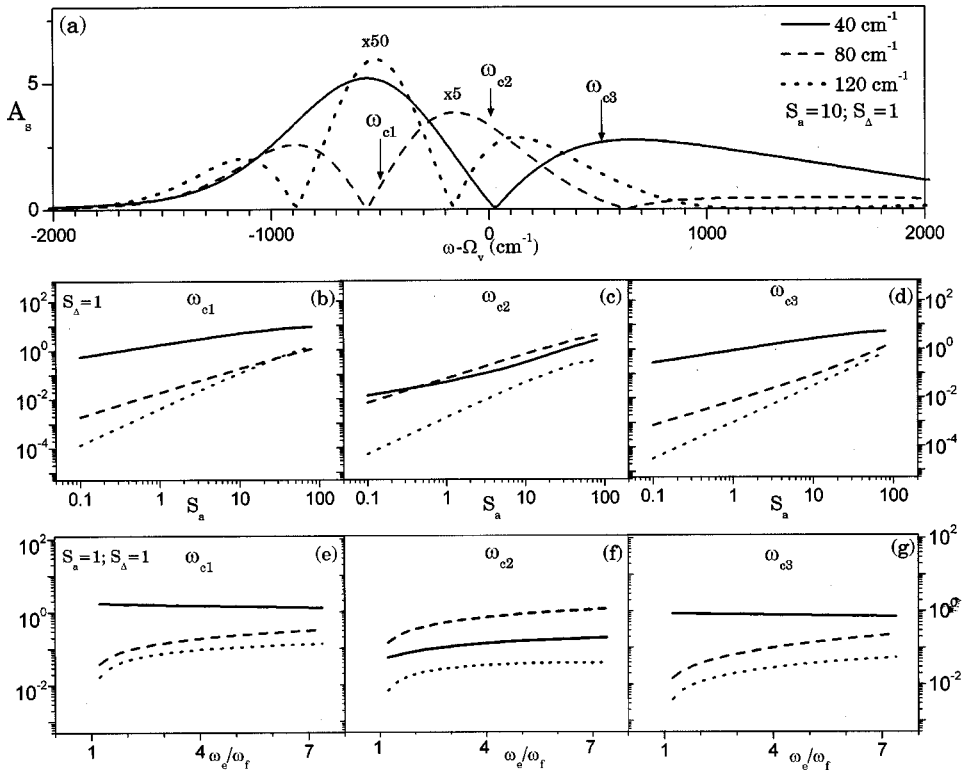

FIG. 9. Simulations of overtone signals from the ground state of Mb using displaced and squeezed states. (a) Amplitude profiles of the fundamental at $40\,\mathrm{cm}^{-1}$ (solid line) and the first two overtones at $80\,\mathrm{cm}^{-1}$ (dashed line) and $120\,\mathrm{cm}^{-1}$ (dotted line), assuming an initial displacement of $S_a=A_g^2/2=10$, and optical coupling strength of $S_\Delta=\Delta^2/2=1$, for the $40\,\mathrm{cm}^{-1}$ mode. Panels (b)–(d) show the amplitudes of the first three harmonics over a wider range of initial displacements, for three carrier frequencies ($\omega_{c1},\omega_{c2},\omega_{c3}$) across the absorption maximum. The corresponding amplitudes of the three harmonics for displaced and squeezed states is plotted in panels (e)–(g), for a wide range of frequency ratios $r=\omega_e/\omega_f$ between the reactant ($|e\rangle$) and product ($|f\rangle$) electronic states.

On the other hand, when the coherence is induced by a nonradiative surface crossing or by intense pump fields,[51,63] the amplitude of the coherent motion can be comparable or larger than the optical coupling strengths, so that the strength of the overtones is expected to be larger. The effective linear response approach using displaced wave packets allows a calculation of pump–probe signals for arbitrary values of the initial amplitude A_g. In order to estimate the strength of overtone signals as a function of A_g, we consider the model line shape of Mb in Fig. 8(f). The overtone signals of a low frequency mode at $40\,\mathrm{cm}^{-1}$ coupled to the optical transition are studied in Fig. 9. The top panel of Fig. 9 shows the profiles of the fundamental and the first two overtones of the $40\,\mathrm{cm}^{-1}$ oscillation, assuming $S_\Delta=\Delta^2/2=1$, and $S_a=A_g^2/2=10$. The contrasting behavior of the overtone and fundamental amplitude profiles is notable from the figure. The fundamental signal amplitude dips near the resonant maximum Ω_v and peaks near the shoulders of the absorption spectrum. The amplitude of the first overtone peaks near Ω_v and vanishes close to the frequency where the fundamental dips. Thus, we can say that the amplitude profiles of the fundamental and the first overtone behave roughly as the first and second derivatives of the equilibrium absorption spectrum. Similarly, the second overtone at $120\,\mathrm{cm}^{-1}$ behaves as the third derivative of the absorption spectrum, vanishing at three different carrier frequencies across the absorption band. Such characteristics are useful for the assignment of overtone oscillations in pump–probe spectroscopy.[35,11]

It is important to note the significant reduction in the amplitude of the overtone oscillations compared to the fundamental. To study the strength of overtone signals over a wider range of initial displacements, we plot in Figs. 9(b)–9(d) the amplitude of the first three harmonics for three different carrier frequencies near resonance. The initial wave packet amplitudes are varied over three orders-of-magnitude and S_Δ is fixed to be unity. It is seen that for detection at the wings of the absorption $\omega_c=\omega_{c1}$ and ω_{c3}, the amplitude of the overtones is more than an order-of-magnitude weaker than the fundamental. This is true even for amplitudes as large as $S_a=100$ (or $A_g\approx 14$). Near band center ω_{c2}, the fundamental signal itself is very small. The first overtone is the dominating contribution even for very small displacements. The almost linear behavior of the overtone amplitudes on the log–log scale suggests a power law dependence of the overtone amplitudes on the wavepacket displacement.

2. Second moment modulation (squeezed states)

While the contribution of the double pass of the wave packet to the intensity of overtone signals is negligible for field driven coherence (see previous section), higher moment modulations of the pump induced wave packet[49] (squeezing) can contribute more significantly to overtone intensities. Overtones signals calculated using the full third-order response approach are found to be much stronger than those calculated with the effective linear response approach using the first moment dynamics. This discrepancy is indicative of the role played by field induced squeezing in the ground state signals. Apart from the laser pulse interaction, squeezing of the nuclear wave packet can also be induced by purely geometrical effects, such as a change in the curvature of the nuclear potentials that are involved in the interaction,[79] i.e., quadratic coupling.

We discuss squeezing in the context of chemical reactions. Introducing quadratic coupling between the potentials of the reactant and product surfaces $|e\rangle$ and $|f\rangle$ shown in Fig.

1, we calculate the probe response to displaced and squeezed dynamics on the product state potential well. For the initial displacement, we continue to use the first moments of the Landau–Zener coherence presented in Appendix B. These were derived assuming linear coupling between the reactant and product surfaces. To obtain the initial conditions of the squeezed state, we adopt a phenomenological view. We assume that the effect of the reaction is to instantly place the thermal equilibrium distribution of the reactant on the product state well. The resulting nonstationary nuclear state is a displaced thermal density matrix that is also squeezed due to the incommensurate thermal widths on the two surfaces. In Appendix D, we have derived an analytic expression for the effective linear response correlation function that describes both the coherent and squeezed dynamics in the ground state.

The central quantity governing the squeezed state dynamics is the ratio of the reactant and product state frequencies $r=(\omega_e/\omega_f)$. It is evident from the effective linear response correlation function Eq. (D6) that squeezed states modulate the equilibrium absorption correlator at even harmonics of the fundamental frequency. We therefore do not expect the fundamental pump–probe signal to be affected significantly by squeezed wave packet dynamics. In Figs. 9(e)–9(g), we simulate the first three harmonics of the $40\,\mathrm{cm}^{-1}$ oscillations, when the wave packet is both displaced and squeezed [the amplitude and phase profiles in the presence of squeezing behave similar to those in Fig. 9(a) and are not plotted]. In the simulations, the initial displacement of the wave packet on the $|f\rangle$ state and the optical coupling are fixed at $S_a=S_\Delta=1$. The squeezing ratio r is varied over a range of 1 to 8. It can be seen that fundamental oscillations are practically unaffected by variations in r. The dramatic effect of squeezing on the overtone amplitude is evident, particularly so for the detection frequency ω_{c2} near the absorption maximum. Here, for squeezing ratios larger than 6, the overtone signal is comparable to the corresponding fundamental signal at the wings of the absorption band $(\omega_{c1},\omega_{c3})$.

The simulations presented in Fig. 9 provide an overall picture of overtone intensities in pump–probe spectroscopy, within a harmonic model with coherent and squeezed initial states. It can be concluded that the fundamental signal is almost always the dominant contribution for reasonable values of wave packet displacement and squeezing. However, when quadratic coupling is also introduced between the electronic levels involved in the probe interaction, i.e., when $\omega_f\neq\omega_{f'}$, the overtone signals are expected to be significantly enhanced. In this case, the strength of the overtone oscillations induced by the curvature change (between the ground and excited state potentials) is coupled to the amplitude of the wave packet motion; larger amplitudes imply that steeper differences in curvature are probed. In contrast, the overtone intensities generated by squeezing the initial wave packet are dependent only on the frequency ratio. A rigorous treatment of the effective linear response functions for a quadratically coupled two-level system will be presented elsewhere.

V. SUMMARY AND CONCLUSIONS

In this work, we have presented a study of the amplitude and phase excitation profiles in femtosecond coherence spectroscopy using an effective linear response approach. In combination with a rigorous moment analysis of the doorway state,[47] the linear response formalism is found to be in excellent agreement with the more complete third-order response formalism.[28] Furthermore, the representation of nonstationary states as displaced thermal states provides a general framework to analyze vibrational coherence induced by nonradiative transitions. We have demonstrated this approach by using the first moments of a quantum coordinate coupled to a Landau–Zener surface crossing.

The effective linear response functions are analytical, and yet retain the correlation function based description (in contrast to the vibronic eigenstates approach)[32,33] implicit in the third-order response formalism. The analytic expressions offer a significant reduction in computation times. Calculations of multiple carrier frequency excitation profiles for arbitrary pulse widths and temperatures are made possible, without the need for semiclassical approximations. A separate moment analysis is also useful in providing clear physical insight into pump–probe signals. Ground state signals generated by impulsive Raman processes exhibit contrasting phase and amplitude behavior from excited state and reaction driven signals.

The ability to incorporate experimentally measured absorption line shapes (and the Kramers–Kronig determined dispersion line shapes) into the pump–probe calculations is another important aspect of the present work. A knowledge of pump–probe excitation profiles and the measured absorption cross sections can be used to extract parameters relevant to a specific mode that is active in pump–probe signals. The use of experimental line shapes eliminates the need for modeling the multimode vibronic mechanisms that cause line broadening. This is analogous to ''transform'' techniques in resonance Raman spectroscopy.[68–70,56] Transform techniques are a powerful means for extracting mode specific information using the measured Raman excitation profiles and the optical absorption profiles on an absolute (cross section) scale.

A study of inhomogeneous broadening in pump–probe signals shows that the ground state amplitude and phase profiles are smeared out by the inhomogeneous broadening. The excited state amplitude dip and phase flip are red shifted with respect to the peak of the emission line shape. A pump–probe analysis of the phase profiles of the $220\,\mathrm{cm}^{-1}$ Fe–His mode in Mb across the Soret band was presented, and was based on a previous model for the strongly asymmetric Soret line shape.[71] The analysis indicates both the ground state origin of the oscillations and the strong inhomogeneous broadening present in Mb. In contrast to the nearly constant phase profile in Mb, the $220\,\mathrm{cm}^{-1}$ mode phase in the reactive sample MbNO shows a clear π phase change near the peak of the transient photoproduct. These results suggest that the $220\,\mathrm{cm}^{-1}$ mode coherence in MbNO arises from the photoproduct Mb. The mode is presumably triggered by the rapid curve crossing occurring during the MbNO photolysis reaction.[14] The absolute phase of the oscillations suggest that

the chemical reaction occurs on a very fast time scale ($\lesssim$20 fs), with the possibility of direct pump pulse involvement at the crossing region in the preparation of the product state coherence.

Although we have not discussed vibrational relaxation in detail, the nonstationary linear response correlation functions in Eqs. (34) and (35) can readily incorporate damped wave packet motion. The initial first moments for the damped oscillator case must however be used instead of the undamped expressions in Appendix A. In the analysis of the oscillatory amplitude and phase profiles, which has been the main subject of the present work, the neglect of damping is justified because the observed modes are weakly damped. However, both under-damped and over damped modes contribute to the nonoscillatory background (offset) in the pump–probe signals.[45,44,20] These offsets can potentially carry important information concerning the equilibrium potential shifts.[20] It is immediately clear from Eqs. (34) and (35) that the modulation of the equilibrium correlator by strongly over-damped or diffusive motion manifests itself as a dynamic, i.e., shifting absorption line shape in the ground state response.[80] Over-damped motion is manifested in the excited state response through phenomena such as fluorescence Stokes-shift dynamics.[28,81] A rigorous analysis of these processes can be readily carried out using the effective linear response approach formalism presented here.

We have also discussed overtone signals in pump–probe spectroscopy using both displaced and squeezed initial states. The contrasting amplitude and phase behavior of the various harmonics are potentially useful for overtone assignments. It is found that for reasonable values of squeezing ratios and wave packet displacements, the fundamental signal is the dominant contribution.

Finally, we mention that the present development can be readily extended beyond the displaced oscillator model. Effective linear response functions can be readily calculated for the case of quadratic electron–nuclear coupling (between the radiatively coupled levels) using standard techniques of quantum field theory. Non-Condon effects can also be incorporated[51,82] into both the pump (moment analysis) and the probe steps. These calculations will be detailed elsewhere.

ACKNOWLEDGMENTS

We thank Dr. T. S. Yang for helpful comments regarding the numerical implementation of the third-order response approach. This work was supported by the National Science Foundation (MCB 9904516) and by the National Institutes of Health (AM 35090).

APPENDIX A: FIRST MOMENTS OF PUMP INDUCED VIBRATIONAL COHERENCE

Consider the ground state doorway $\delta\hat{\rho}_g$ in Eq. (23). Let the pump field be of the form $E_a(t)=E_0G(t)\cos(\omega_c t)$ where $G(t)$ is a dimensionless envelope function, and E_0 is the electric field strength of the pump pulse. General expressions have been derived for all the moments of $\hat{Q}$ and $\hat{P}$ for the density matrix $\delta\hat{\rho}_g$ using moment generating functions, and related to equilibrium line shape functions.[47] The first moments of $\hat{Q}$ and $\hat{P}$ are found to be (in dimensionless units)

$$Q_{g0}=-\frac{|\mu_{ge}|^2E_0^2(2\bar{n}+1)\Delta}{8\pi\hbar^2N_g'}\times\int_0^\infty d\omega\,\tilde{G}_p(\omega-\omega_c,-\omega_0)\hat{\Delta}\Phi_I(\omega), \tag{A1}$$

$$P_{g0}=\frac{|\mu_{ge}|^2E_0^2\Delta}{8\pi\hbar^2N_g'}\int_0^\infty d\omega\,\tilde{G}_p(\omega-\omega_c,-\omega_0)\hat{\Delta}\Phi_R(\omega). \tag{A2}$$

Here, $N_g'=1-\mathrm{Tr}[\delta\hat{\rho}_g]$ is the net ground state population after the pump interaction, and $\Phi_I(\omega)$ and $\Phi_R(\omega)$ are the imaginary and the real parts of the complex equilibrium lineshape function defined in Eq. (29). $\tilde{G}_p(\omega-\omega_c,-\omega_0)$ is the product spectral function defined in Eq. (41). The action of the operator $\hat{\Delta}$ (not to be confused with the dimensionless excited state potential shift Δ) is to generate differences: $\hat{\Delta}\Phi_I(\omega)=\Phi_I(\omega)-\Phi_I(\omega-\omega_0)$. With the initial position and momentum increments given in Eqs. (A1) and (A2), the time-dependent first moment dynamics in the ground state is given rigorously as the solution to the damped oscillator equation

$$\bar{Q}_g(s)=A_ge^{-\gamma|s|}\cos(\omega_v s+\varphi_g), \tag{A3}$$

where γ and $\omega_v=\sqrt{\omega_0^2-\gamma^2}$ are the damping constant and effective frequency of the mode. The amplitude and phase are given by $A_g=\sqrt{Q_{g0}^2+P_{g0}^2}$ and $\varphi_g=-\tan^{-1}[P_{g0}/Q_{g0}]$.

The various moments of $\hat{Q}$ and $\hat{P}$ for the excited state doorway $\delta\hat{\rho}_e$ in Eq. (26) can also be obtained. It is found[47] that the excited nuclei receive no initial momentum i.e., $P_{e0}=0$. The mean position (with respect to the excited state potential equilibrium Δ) is given by

$$Q_{e0}=-\frac{|\mu_{ge}|^2E_0^2\Delta}{4\pi\hbar^2N_e'}\int_0^\infty d\omega\,\tilde{G}_p(\omega-\omega_c,-\omega_0)\times[\Phi_I(\omega-\omega_0)-\bar{n}\hat{\Delta}\Phi_I(\omega)], \tag{A4}$$

where $N_e'=\mathrm{Tr}[\delta\hat{\rho}_e]$ is the electronic population in the excited state ($N_g'+N_e'=1$). Thus, the amplitude for the excited state coherent motion is given by $A_e=|Q_{e0}|$, and the time-dependent first moment is

$$\bar{Q}_e(s)=Q_{e0}e^{-\gamma|s|}\cos(\omega_v s). \tag{A5}$$

APPENDIX B: FIRST MOMENTS OF COHERENCE DRIVEN BY LANDAU–ZENER SURFACE CROSSING

We consider a product electronic state $|f\rangle$ that is coupled nonradiatively to the reactant excited state $|e\rangle$ as in Fig. 1(b). The Hamiltonian of the problem consists of the 2×2 lower block diagonal matrix of $\hat{H}_{\mathrm{NR}}$ in Eq. (46). The system is assumed to be initially ($t=0$) in thermal equilibrium along the quantum mechanical degrees of freedom of the state $|e\rangle$. The nonradiative coupling J will induce a transition to the state $|f\rangle$. The time-dependent surface crossing along the classical reaction coordinate R will be accompanied by quan-

tum mechanical tunneling between the vibrational levels of $\hat{H}_e$ and $\hat{H}_f$. The time-dependent quantum yield for the transition $e \rightarrow f$ can be shown to be

$$P_{ef}(t) = 1 - \exp\left\{ - \int_0^t ds\, \mathcal{G}(R(s)) \right\}. \tag{B1}$$

Here, $\mathcal{G}(R(s))$ is the Fermi Golden rule transition rate for making an electronic transition from the state $|e\rangle$ to the electronic state $|f\rangle$ and is expressed as[21]

$$\mathcal{G}(R(s)) = \frac{2\pi J^2}{\hbar^2} \Phi_I^{ef}(\omega = 0, \Omega_{00}^{ef}(R(s))). \tag{B2}$$

$\Omega_{00}^{ef}(R(s)) = U_f(R(s)) - U_e(R(s))$ is the time-dependent energy gap between the e and f states. $\Phi_I^{ef}(\omega)$ is the spectral absorption line shape function for the $e \rightarrow f$ electronic transition, obtained using Eqs. (27)–(29) with Ω_{00} replaced by $\Omega_{00}^{ef}(R(s))$. In the single mode limit, i.e., no Q coupling, Eq. (B2) yields a delta function. The time-dependent quantum yield $P_{ef}(t)$ will then be a simple step function in time. The presence of additional degrees of freedom smears out the curve crossing process and can be completely described by the zero frequency component of the spectral line shape function $\Phi_I^{ef}(\omega)$.

The time-dependent surface crossing along the R coordinate induces oscillations along Q, which is initially in thermal equilibrium. It can be shown generally that the mean position of the oscillator in the product state obeys[21]

$$\overline{Q}_f(t) = \frac{\omega_0^2 \Delta_{ef}}{\omega_v} \int_0^\infty ds e^{-\gamma s} \sin(\omega_v s) P_{ef}(t-s). \tag{B3}$$

Here, γ is the vibrational damping, Δ_{ef} is the dimensionless shift between the e and f oscillators, and $\omega_v = \sqrt{\omega_0^2 - \gamma^2}$. The above equation rigorously describes the first moment of the nuclear dynamics on the product state well, with the one qualification that it is valid only at times t when the system has made its transition into the product state, i.e., $P_{ef}(t) = 1$. When $P_{ef}(t) < 1$, $\overline{Q}_f(t)$ consists of oscillations in both the reactant and product surfaces and is more difficult to interpret. We can recast Eq. (B3) to a form that readily yields the initial conditions for the probe, i.e., detection step. Integrating Eq. (B3) by parts, we get in the long time limit [assuming $P_{ef}(\infty) = 1$]

$$\overline{Q}_f(t) = \Delta_{ef} + A_f e^{-\gamma t} \cos(\omega_v t + \varphi_f), \tag{B4}$$

where

$$A_f \cos(\varphi_f) = -\Delta_{ef} \int_{-\infty}^\infty dt' \dot{P}_{ef}(t') e^{\gamma t'} \times [\cos(\omega_v t') - (\gamma/\omega_v) \sin(\omega_v t')], \tag{B5}$$

$$A_f \sin(\varphi_f) = \Delta_{ef} \int_{-\infty}^\infty dt' \dot{P}_{ef}(t') e^{\gamma t'} \times [\sin(\omega_v t') + (\gamma/\omega_v) \cos(\omega_v t')]. \tag{B6}$$

Equations (B5) and (B6) determine the amplitude and phase of the oscillatory motion induced by the surface crossing. They can be readily incorporated into the probe step using a displaced thermal state representation. The above expressions depend on the reaction parameters $[J, \beta, \Omega_{00}^{ef}(R)$, etc.] through $P_{ef}(t)$ and Eq. (B1). Extension of the multidimensional Landau–Zener theory to incorporate nonstationary initial conditions along the Q degree of freedom can be carried out using displaced thermal density matrices, with the displacements obtained from the excited state first moment presented in Appendix A.

APPENDIX C: NONLINEAR RESPONSE FUNCTIONS

When the ground state doorway $\delta\hat{\rho}_g$ in Eq. (23) is substituted in the expression for $C_g(t,t_3)$ in Eq. (22), we are left with the thermal average of a four-time correlation function. The average can be evaluated exactly using a second-order cumulant expansion, and the result is

$$C_g(t,t_3) = -\frac{\mu^2}{\hbar^2} \int_{-\infty}^\infty dt_2 \int_{-\infty}^{t_2} dt_1 E_a(t_1) E_a(t_2) \times [R_4(t,t_3,t_2,t_1) + R_3(t,t_3,t_2,t_1)]. \tag{C1}$$

Here, R_3 and R_4 are the nonlinear response functions given by,[83,26,28]

$$R_3(t,t_1,t_2,t_3) = \mathcal{H}(t-t_3)\mathcal{H}(t_2-t_1) e^{-i\Omega_{00}(t-t_3-t_2+t_1)} \times e^{-g(t-t_3) - g^*(t_2-t_1) + f_2^*(t,t_1,t_2,t_3)}, \tag{C2a}$$

$$R_4(t,t_1,t_2,t_3) = \mathcal{H}(t-t_3)\mathcal{H}(t_2-t_1) e^{-i\Omega_{00}(t-t_3+t_2-t_1)} \times e^{-g(t-t_3) - g(t_2-t_1) - f_2(t,t_1,t_2,t_3)}, \tag{C2b}$$

where we have defined

$$f_2(t,t_1,t_2,t_3) = g(t-t_1) - g(t-t_2) + g(t_3-t_2) - g(t_3-t_1). \tag{C3}$$

The function $\mathcal{H}(t)$ accounts for homogeneous broadening and is typically of the form $e^{-\Gamma_e |t|}$, Γ_e being the homogeneous damping constant. In these expressions, $t_2 - t_1$ reflects the time interval when the system is in an electronic coherence during the pump field interaction, whereas $t - t_3$ is the time interval when the system is in an electronic coherence during the probe interaction.[28] Thus, $\mathcal{H}(t)$ appears separately for the pump and the probe interactions.

Turning to the excited state response, substitution of $\delta\hat{\rho}_e$ in Eq. (26) into the expression for C_e in Eq. (25) and using a second-order cumulant expansion, we find

$$C_e(t,t_3) = \frac{\mu^2}{\hbar^2} \int_{-\infty}^\infty dt_2 \int_{-\infty}^{t_2} dt_1 E_a(t_1) E_a(t_2) \times [R_1^*(t,t_1,t_2,t_3) + R_2^*(t,t_1,t_2,t_3)]. \tag{C4}$$

Here, R_1 and R_2 are the nonlinear response functions given by[26,28]

$$R_1(t,t_1,t_2,t_3) = \mathcal{H}(t-t_3)\mathcal{H}(t_2-t_1) e^{-i\Omega_{00}(t-t_3+t_2-t_1)} \times e^{-g^*(t-t_3) - g(t_2-t_1) - f_1(t,t_1,t_2,t_3)}, \tag{C5a}$$

$$R_2(t,t_1,t_2,t_3) = \mathcal{H}(t-t_3)\mathcal{H}(t_2-t_1) e^{-i\Omega_{00}(t-t_3-t_2+t_1)} \times e^{-g^*(t-t_3) - g^*(t_2-t_1) + f_1^*(t,t_1,t_2,t_3)}, \tag{C5b}$$

and we have defined

$$f_1(t,t_1,t_2,t_3)=g(t-t_1)-g^*(t-t_2)$$
$$-g(t_3-t_1)+g^*(t_3-t_2). \tag{C6}$$

In the above expressions $g(s)$ is the harmonic oscillator correlation function [Eq. (28)].

Equations (C1) and (C4) express the two-time effective linear response correlation functions $C_{g,e}(t,t_3)$ as as convolution of the well-known nonlinear response functions[8,28] R_j $(j=1...4)$ with the two pump field interactions. The convolution with the pump laser fields implicitly takes into account the complete information about the nonstationary state of the system expressed by the density matrices $\delta\hat{\rho}_g$ and $\delta\hat{\rho}_e$. It is worth noting here that both $C_g(t,t_3)$ and $C_e(t,t_3)$ can be factored into equilibrium and nonequilibrium parts as follows:

$$C_g(t,t_3)=K_g(t-t_3)C_g'(t,t_3);$$
$$C_e(t,t_3)=K_e(t-t_3)C_e'(t,t_3), \tag{C7}$$

where $K_g(t-t_3)$ and $K_e(t-t_3)$ are given by Eq. (27).

Inhomogeneous broadening due to a static distribution $\mathcal{F}_I(\Omega_{00})$ can be incorporated into the above expressions. The correlation functions C_g and C_e must be averaged with respect to the inhomogeneous distribution. The electronic energy gap appears in the response functions R_j through the oscillatory factors $e^{-i\Omega_{00}[(t-t_3)\pm(t_2-t_1)]}$. The averaging over $\mathcal{F}_I(\Omega_{00})$ thus involves a simple Fourier transform and can be carried out independently of the time integrations. The resulting inhomogeneous response functions $R_j^{(I)}$ can then be expressed in terms of the homogeneous ones R_j in the following factorized form:[28]

$$R_{1,4}^{(I)}(t,t_1,t_2,t_3)=R_{1,4}(t,t_1,t_2,t_3)\tilde{\mathcal{F}}_I(t-t_3+t_2-t_1), \tag{C8a}$$

$$R_{2,3}^{(I)}(t,t_1,t_2,t_3)=R_{2,3}(t,t_1,t_2,t_3)\tilde{\mathcal{F}}_I(t-t_3-t_2+t_1), \tag{C8b}$$

where $\tilde{\mathcal{F}}_I(t)$ is the Fourier transform of the inhomogeneous distribution $\mathcal{F}_I(\Omega_{00})$.

APPENDIX D: EFFECTIVE LINEAR RESPONSE FUNCTION FOR A TWO-LEVEL SYSTEM WITH SQUEEZED VIBRATIONAL STATES

Consider two nonradiatively coupled reactant $|e\rangle$ and product $|f\rangle$ electronic states. Let the vibrational potentials be harmonic with linear and quadratic coupling, with frequencies ω_e and ω_f. Since two different vibrational frequencies are involved, we will first use dimensional units for clarity and will revert to dimensionless units later. Just before the reaction, the system is in thermal equilibrium on the electronic state $|e\rangle$ with the coordinate and momentum uncertainties $(\sigma_A^2=\langle\hat{A}^2\rangle-\langle\hat{A}\rangle^2)$ given by

$$\sigma_{Qe}^2=(\hbar/2m\omega_e)(2\overline{n}_T+1);\sigma_{Pe}^2=(m\omega_e\hbar/2)(2\overline{n}_T+1), \tag{D1}$$

where $\overline{n}_T$ is the mean occupation number at temperature T. The position and momentum uncertainties in the product state are obtained from the above expression by simply replacing ω_e by ω_f. If we picture the chemical reaction as instantly creating distributions of the above widths in the product state well, the initial nonequilibrium state in the product well will appear to be squeezed in the position and momentum coordinates. The nonstationary state can be generated from the thermal equilibrium density matrix of the product well by the squeezing operator defined as[40]

$$\hat{S}(\beta)=\exp\left[\frac{\beta}{2}(\hat{a}^{\dagger 2}-\hat{a}^2)\right];\beta=-\frac{1}{2}\ln\left(\frac{\omega_f}{\omega_e}\right). \tag{D2}$$

The present choice of the squeezing operator maintains the minimum uncertainty product. Arbitrary changes in the uncertainty product can be incorporated[40] by a complex value for the squeezing parameter β, but is not considered here for simplicity. It is easy to verify that the unitary operator $\hat{S}(\beta)$ converts the thermal density matrix for the state $|f\rangle$, i.e., $\hat{\rho}_T^{(f)}$ to the thermal density matrix for the state $|e\rangle$, i.e., $\hat{\rho}_T^{(e)}$. The position and momentum uncertainties are also changed to the thermal values in the reactant state given in Eq. (D1).

Since the wave packet induced in the state $|f\rangle$ is in general both displaced and squeezed, we may represent the corresponding density matrix as

$$\hat{\rho}_f'=\hat{D}(\lambda_f)\hat{S}(\beta)\hat{\rho}_T^{(f)}\hat{S}^\dagger(\beta)\hat{D}^\dagger(\lambda_f). \tag{D3}$$

With the above representation, we evaluate the correlation function similar to Eq. (22). We find [reverting to dimensionless units where the scaling factor is $(\hbar/m\omega_f)^{1/2}$]

$$C_f(t,t_3)=e^{-i\Omega_v^f(t-t_3)}Tr\left[\hat{\rho}_T^{(f)}\exp\left(i\omega_f\Delta\int_{t_3}^{t}ds\,\hat{S}^\dagger(\beta)\right.\right.$$
$$\left.\left.\times\hat{D}^\dagger(\lambda_f)\hat{Q}(s)\hat{D}(\lambda_f)\hat{S}(\beta)\right)_+\right], \tag{D4}$$

where we have used the invariance of trace under cyclic permutation to bring the unitary operators inside the time ordered exponential. Using the properties of coherent and squeezed states,[40] we have

$$\hat{S}^\dagger(\beta)\hat{D}^\dagger(\lambda_f)\hat{Q}(s)\hat{D}^\dagger(\lambda_f)\hat{S}(\beta)$$
$$=A_f\cos(\omega_f s+\varphi_f)+(\hat{a}\Lambda(s)+\hat{a}^\dagger\Lambda^*(s)), \tag{D5}$$

where $\Lambda(s)=(\cosh(\beta)e^{-i\omega_f s}+\sinh(\beta)e^{i\omega_f s})$. Substituting this in Eq. (D4), we can remove the c-number displacement outside the time ordering. The resulting thermal average can be evaluated exactly using Wick's theorem. We finally obtain

$$C_f(t,t_3)=K_f(t-t_3)\exp[iA_f\Delta(\sin(\omega_f t+\varphi_f)$$
$$-\sin(\omega_f t_3+\varphi_f))]\exp[-R(2\cos(\omega_f(t+t_3))$$
$$-\cos(2\omega_f t)-\cos(2\omega_f t_3))], \tag{D6}$$

where we have defined

$$R=\frac{\Delta^2}{2}(2\overline{n}_T+1)\cosh(\beta)\sinh(\beta)=\frac{(2\overline{n}_T+1)\Delta^2(r^2-1)}{8r}. \tag{D7}$$

Here, $r=\omega_e/\omega_f$ and Δ is the dimensionless shift between the product ground and excited potentials. The equilibrium correlator is given by $K_f(t-t_3)=e^{-i\Omega_{00}^f}e^{-g(t-t_3)}$, where $g(s)$ now takes a slightly different form as compared to Eq. (28):

$$g(t-t_3)=\frac{\Delta_f^2}{2}[(2\overline{n}_T'+1)(1-\cos(\omega_f(t-t_3)))$$
$$+i\sin(\omega_f(t-t_3))], \tag{D8}$$

where

$$(2\overline{n}_T'+1)=\coth(\hbar\omega_f/2k_BT)(\cosh^2(\beta)+\sinh^2(\beta)). \tag{D9}$$

Equation (D6) expresses the nonequilibrium response as the modulation of the equilibrium correlator $K_f(t-t_3)$ by the coherent and squeezed dynamics of the nuclear motion on the ground electronic state $|f\rangle$ of the product. In addition to the exponential factor that describes coherent dynamics, squeezing introduces an additional factor that modulates at the even harmonics of the fundamental oscillator frequency ω_f. It is seen that the strength of the overtone modulations are determined by the factor R defined in Eq. (D7). We also note that the effect of a squeezed initial state *on the equilibrium part* of the correlator is to change the effective temperature as in Eq. (D9).

[1] M. J. Rosker, F. W. Wise, and C. L. Tang, Phys. Rev. Lett. **57**, 321 (1986).
[2] S. Ruhman, A. G. Joly, and K. A. Nelson, J. Chem. Phys. **86**, 6563 (1987).
[3] Y. Yan and K. A. Nelson, J. Chem. Phys. **87**, 6240 (1987).
[4] Y. Yan and K. Nelson, J. Chem. Phys. **87**, 6257 (1987).
[5] A. H. Zewail, Science **242**, 1645 (1988).
[6] H. L. Fragnito, J. Y. Bigot, P. C. Becker, and C. V. Shank, Chem. Phys. Lett. **160**, 101 (1989).
[7] N. F. Scherer, R. J. Carlson, A. Matro, M. Du, A. J. Ruggeiro, V. R. Rochin, J. A. Cina, G. R. Fleming, and S. A. Rice, J. Chem. Phys. **95**, 1487 (1991).
[8] W. T. Pollard and R. A. Mathies, Annu. Rev. Phys. Chem. **43**, 497 (1992).
[9] S. L. Dexheimer, Q. Wang, L. A. Peteanu, W. T. Pollard, R. A. Mathies, and C. V. Shank, Chem. Phys. Lett. **188**, 61 (1992).
[10] A. Zewail, J. Phys. Chem. **97**, 12427 (1993).
[11] M. H. Vos, F. Rappaport, J. C. Lambry, J. Breton, and J. L. Martin, Nature (London) **363**, 320 (1993).
[12] T. P. Doughery, G. P. Weiderrecht, K. A. Nelson, M. H. Garret, H. P. Jensen, and C. Warde, Science **258**, 770 (1992).
[13] L. Dhar, J. A. Rogers, and K. A. Nelson, Chem. Rev. **94**, 157 (1994).
[14] L. Zhu, J. T. Sage, and P. M. Champion, Science **266**, 629 (1994).
[15] Q. Wang, R. W. Schoenlein, L. A. Peteanu, R. A. Mathies, and C. V. Shank, Science **266**, 422 (1994).
[16] S. E. Bradforth, T. Jiminez, F. V. Mourik, R. V. Grondelle, and G. R. Fleming, J. Phys. Chem. **99**, 16179 (1995).
[17] D. M. Jonas, M. J. Lang, Y. Nagasawa, T. Joo, and G. R. Fleming, J. Phys. Chem. **100**, 12660 (1996).
[18] M. Chachisvilis and V. Sundstrom, J. Chem. Phys. **104**, 5734 (1996).
[19] M. Chachisvilis and V. Sundstrom, Chem. Phys. Lett. **234**, 141 (1995).
[20] T. S. Yang, M. S. Chang, M. Hayashi, S. H. Lin, P. Vohringer, W. Dietz, and N. F. Scherer, J. Chem. Phys. **110**, 12070 (1999).
[21] L. Zhu, A. Widom, and P. M. Champion, J. Chem. Phys. **107**, 2859 (1997).
[22] D. D. Schuresco and W. W. Webb, Biophys. J. **24**, 382 (1978).
[23] Q. H. Gibson, J. S. Olson, R. E. Mckinnie, and R. J. Rohlfs, J. Biol. Chem. **261**, 10228 (1986).
[24] L. M. Miller, A. J. Pedraza, and M. R. Chance, Biochemistry **36**, 12199 (1997).
[25] R. W. Hellwarth, Prog. Quantum Electron. **5**, 1 (1977).
[26] S. Mukamel, Phys. Rep. **93**, 1 (1982).
[27] W. T. Pollard, S. L. Dexheimer, Q. Wang, L. A. Peteanu, C. V. Shank, and R. A. Mathies, J. Phys. Chem. **96**, 6147 (1992).
[28] S. Mukamel, *Principles of Nonlinear Optical Spectroscopy* (Oxford University Press, New York, 1995).
[29] Y. J. Yan, L. E. Fried, and S. Mukamel, J. Phys. Chem. **93**, 8149 (1989).
[30] Y. J. Yan and S. Mukamel, Phys. Rev. A **41**, 6485 (1990).
[31] S. Mukamel, Annu. Rev. Phys. Chem. **41**, 647 (1990).
[32] B. Fain and S. Lin, Chem. Phys. **161**, 515 (1992).
[33] B. Fain, S. Lin, and V. Khidekel, Phys. Rev. A **47**, 3222 (1993).
[34] B. Fain and S. Lin, Chem. Phys. Lett. **207**, 287 (1993).
[35] F. Rosca, A. T. N. Kumar, X. Ye, T. Sjodin, A. A. Demidov, and P. M. Champion, J. Phys. Chem. **104**, 4280 (2000).
[36] R. D. Coalson, D. G. Evans, and A. Nitzan, J. Chem. Phys. **101**, 436 (1994).
[37] M. Cho and R. J. Silbey, J. Chem. Phys. **103**, 595 (1995).
[38] W. Domcke and G. Stock, Adv. Chem. Phys. **100**, 1 (1997).
[39] S. Dilthey, S. Hahn, and G. Stock, J. Chem. Phys. **112**, 4910 (2000).
[40] L. Mandel and E. Wolf, *Optical Coherence and Quantum Optics* (Cambridge University Press, Cambridge, 1995).
[41] J. A. Cina and T. J. Smith, J. Chem. Phys. **98**, 9211 (1993).
[42] M. Cho, G. R. Fleming, and S. Mukamel, J. Chem. Phys. **98**, 5314 (1993).
[43] M. Cho, M. Du, N. F. Scherer, G. R. Fleming, and S. Mukamel, J. Chem. Phys. **99**, 2410 (1993).
[44] D. M. Jonas, S. Bradforth, S. Passino, and G. R. Fleming, J. Phys. Chem. **99**, 2594 (1995).
[45] T. J. Smith, L. Ungar, and J. A. Cina, J. Lumin. **58**, 66 (1994).
[46] Y. C. Shen and J. A. Cina, J. Chem. Phys. **110**, 9793 (1999).
[47] A. T. N. Kumar, F. Rosca, A. Widom, and P. M. Champion (submitted).
[48] J. J. Sakurai, *Modern Quantum Mechanics*, revised ed. (Addison Wesley, Reading, MA, 1994).
[49] B. Fain and S. Lin, J. Chem. Phys. **93**, 6387 (1990).
[50] P. C. Martin, *Measurements and Correlation Functions* (Gordon and Breach, New York, 1968).
[51] U. Banin, A. Bartana, S. Ruhman, and R. Kosloff, J. Chem. Phys. **101**, 8461 (1994).
[52] Y. Tanimura and S. Mukamel, J. Opt. Soc. Am. B **10**, 2263 (1993).
[53] T. J. Dunn, I. A. Walmsley, and S. Mukamel, Phys. Rev. Lett. **74**, 884 (1995).
[54] The displacement operator is the generator of coherent states of the harmonic oscillator from the vacuum state. Coherent states are the nearest approximation to classical states of the oscillator, and derive their name due to their quantum statistical properties. See for example, J. R. Klauder and E. C. G. Sudarshan, *Fundamentals of quantum optics* (Benjamin, New York, 1968).
[55] L. D. Zeigler, R. Fan, A. Desrosiers, and N. F. Scherer, J. Chem. Phys. **100**, 1823 (1994).
[56] J. B. Page, in *Light Scattering in Solids VI*, edited by M. Cardona and G. Guntherodt (Springer, Berlin, 1991), p. 17.
[57] Y. Gu, A. Widom, and P. M. Champion, J. Chem. Phys. **100**, 2547 (1994).
[58] Note that the normalization factor necessary to account for the pump induced electronic population change of the ground and excited states, i.e., the trace of $\delta\hat{\rho}_g$ and $\delta\hat{\rho}_e$ [which are unchanged in the representation Eq. (30) due to the unitarity of the displacement operator] is not shown for simplicity.
[59] S. Druet and J. E. Taran, Prog. Quantum Electron. **7**, 1 (1981).
[60] A. M. Walsh and R. F. Loring, Chem. Phys. Lett. **160**, 299 (1989).
[61] Note that the RWA employed in the derivation of Eqs. (38)–(44) is still valid in the off-resonant region, where the real part of the line shape dominates the imaginary part. However, it is straightforward to include non-RWA terms in the calculation, and the expressions will now also involve the line shapes at negative frequencies; i.e., $\Phi_R(-\omega)$ and $\Phi_I(-\omega)$.
[62] S. Constantine, Y. Zhou, J. Morais, and L. D. Zeigler, J. Phys. Chem. **101**, 5456 (1997).
[63] T. J. Smith and J. A. Cina, J. Chem. Phys. **104**, 1272 (1996).
[64] W. Pollard, S. Lee, and R. Mathies, J. Chem. Phys. **92**, 4012 (1990).
[65] S. L. Dexheimer, A. D. V. Pelt, J. A. Brozik, and B. I. Swanson, J. Phys. Chem. A **104**, 4308 (2000).
[66] Y. Zhou, S. Constantine, S. Harrel, and L. D. Zeigler, J. Chem. Phys. **110**, 5893 (1999).
[67] For a multimode system, it is found that the pump–probe excitation profiles for a given mode depend weakly on the nonequilibrium displacements of the rest of the optically coupled modes. This is to be contrasted with the Raman excitation profile, which depends only on the parameters specific to a given mode, with the rest of the modes in the system implicitly carried through in the equilibrium line shape functions (Ref. 68).
[68] J. B. Page and D. Tonks, J. Chem. Phys. **75**, 5694 (1981).
[69] B. R. Stallard, P. M. Champion, P. Callis, and A. C. Albrecht, J. Chem. Phys. **78**, 712 (1983).
[70] K. T. Schomacker and P. M. Champion, J. Chem. Phys. **90**, 5982 (1989).
[71] V. Srajer, K. T. Schomacker, and P. M. Champion, Phys. Rev. Lett. **57**, 1267 (1986).

[72] W. E. Moerner and T. Basche, Angew. Chem. **105**, 537 (1993).
[73] P. C. Becker, H. L. Fragnito, J. Y. Bigot, C. H. Brito-Crux, R. L. Fork, and C. V. Shank, Phys. Rev. Lett. **63**, 505 (1989).
[74] R. I. Personov, E. I. Al'Shits, and L. A. Bykovskaya, Opt. Commun. **6**, 169 (1972).
[75] P. M. Champion, J. Raman Spectrosc. **23**, 557 (1992).
[76] P. M. Champion and R. Lange, J. Chem. Phys. **73**, 5947 (1980).
[77] V. Srajer, Ph.D. thesis, Northeastern University, 1991.
[78] S. S. Stavrov, Biophys. J. **65**, 1942 (1993).
[79] J. Janszky, A. Vinogradov, I. Walmsley, and J. Mostowski, Phys. Rev. A **50**, 732 (1994).
[80] A. Demidov *et al.* (unpublished).
[81] L. W. Ungar and J. A. Cina, Adv. Chem. Phys. **100**, 171 (1997).
[82] V. Khidekel, V. Chernyak, and S. Mukamel, J. Chem. Phys. **105**, 8543 (1996).
[83] The notation for the response functions here is chosen to be consistent with previous work (Ref. 28). Note that the temporal variables used here are different from those on p. 213 of Ref. 28 through a simple change of variables according to $t_3 \rightarrow t - t_3$, $t_2 \rightarrow t - t_2 - t_3$, and $t_1 \rightarrow t - t_1 - t_2 - t_3$.